This is a preprint of the following article, which is available from mdolab.engin.umich.edu
Jonsson, E., Riso, C., Gray, Monteiro. B. B., Gray, A. C., Martins, J. R. R. A., and Cesnik, C. E. S., High-fidelity Aerostructural Optimization with a Geometrically Nonlinear Flutter Constraint, *AIAA Journal*, April 2023.
The original article may differ from this preprint and is available at
https://doi.org/10.2514/1.J061575.

High-Fidelity Gradient-Based Wing Structural Optimization Including Geometrically Nonlinear Flutter Constraint

Eirikur Jonsson[1,*], Cristina Riso[2], Bernardo Bahia Monteiro[1], Alasdair C. Gray[1], Joaquim R. R. A. Martins[1], and Carlos E. S. Cesnik[1]
[1] *University of Michigan, Ann Arbor, MI, 48109*
[2] *Georgia Institute of Technology, Atlanta, GA, 30332*

Abstract

Lightweight, high-aspect-ratio wings make aircraft more energy efficient thanks to their lower induced drag. Because such wings exhibit large deflections, design optimization based on linear flutter analysis of the wing undeformed shape is inadequate. To address this issue, we develop a framework for integrating a geometrically nonlinear flutter constraint, which considers in-flight deflections, into a high-fidelity gradient-based structural optimization. The wing mass and stress constraints are evaluated on a linear, built-up (detailed) finite element model to capture realistic structural features. The geometrically nonlinear flutter constraint is based on a condensed low-order beam representation of the built-up finite element model, which captures the impact of in-flight deflections with tractable computational effort for optimization. The flutter constraint is differentiated with respect to the detailed structural model sizing variables using the adjoint method to enable large-scale optimizations. The framework is demonstrated by minimizing the mass of a wingbox model subject to the geometrically nonlinear flutter constraint along with stress and adjacency constraints. The geometrically nonlinear flutter constraint adds a penalty up to 60% of the baseline mass due to the impact of in-flight deflections on the flutter onset speed and its mechanism. In contrast, a linear flutter constraint evaluated on the undeformed wing adds a mass penalty of only 10%. This methodology can help design energy-efficient aircraft with high-aspect-ratio wings, which require geometrically nonlinear flutter analyses early in the design cycle.

1 Introduction

Climate change concerns motivate aircraft with lightweight, high-aspect-ratio wings for higher energy efficiency [1]. These aircraft can mitigate aviation environmental impacts, but challenge standard design practices based on linear aeroelasticity techniques [2]. These techniques are inapplicable to high-aspect-ratio wings because their large in-flight deflections invalidate the small displacement assumptions of linear aeroelastic models. The geometrically nonlinear effects associated with large deflections may cause flutter at flight conditions expected to be stable from the

[1]Corresponding author: eirikurj@umich.edu

linear flutter analysis of the undeformed wing. Additionally, they may also change the critical flutter mode, which greatly affects the design modifications used to suppress flutter onset [3–7]. Therefore, the flutter boundaries of high-aspect-ratio-wing (HARW) aircraft must be computed earlier in the design cycle, accounting for in-flight deflections in the flutter analysis.

A promising approach to consider flutter early in the design cycle of high-aspect-ratio-wing aircraft is to add a flutter constraint to a design optimization process [8]. This approach can produce energy-efficient designs requiring fewer late modifications by ensuring adequate flutter margins while minimizing mass or fuel burn. Despite the progress in flutter-constrained aircraft design optimization [8], most previous efforts have used linear flutter analyses of the undeformed wing, or have only included aerodynamic nonlinear effects due to transonic flow [9–11].

Flutter analyses based on the undeformed wing are accurate only as long as in-flight deflections are small enough not to alter the wing's structural and aerodynamic characteristics, which may shift the flutter onset speed or change the flutter mechanism. Because high-aspect-ratio wings undergo large deflections under normal operating loads, they require a geometrically nonlinear flutter analysis process that accounts for the impact of in-flight deflections [2], which vary with the flight condition. Such a geometrically nonlinear process consists of: (1) computing the wing's nonlinear static aeroelastic equilibria at the flight conditions of interest; (2) linearizing the equations of motion about the obtained equilibrium states; (3) extracting the aeroelastic eigenvalues of the local linearized systems; and (4) using the obtained aeroelastic eigenvalue to compute the flutter boundary.

Werter and De Breuker [12] applied this geometrically nonlinear approach in their aeroelastic optimization framework PROTEUS. Their aeroelastic model consists of a geometrically nonlinear beam, with parametrized cross-sectional geometry, coupled to an unsteady vortex lattice model. PROTEUS has been used for aeroelastic optimization in previous work, minimizing structural mass subject to constraints on flutter and structural failure under both static and dynamic loads [13, 14]. Variyar *et al.* [15] minimized the fuel burn of a strut-braced-wing aircraft subject to a geometrically nonlinear flutter speed constraint along with maneuver and gust constraints. They found that the flutter constraint drove their optimized design, causing a fuel burn penalty compared with the case of only maneuver and gust constraints. Xie *et al.* [16] optimized the weight of a wind-tunnel wing to make it flutter in a given speed range, observing different results with and without considering wing deflections in the flutter analysis. Lupp and Cesnik [17] minimized the fuel burn of a blended-wing-body aircraft subject to a stress constraint and a damping-based linear or geometrically nonlinear flutter constraint. They showed that the flutter constraint adds a fuel burn penalty, which increases when considering geometrically nonlinear effects.

These studies highlighted the need for geometrically nonlinear flutter analyses in aircraft design optimization when minimizing objective functions that favor higher wing aspect ratios, such fuel burn. However, the studies evaluated not only flutter, but also the other functions of interest using beam models. These models capture the impact of wing in-flight deflections on the flutter boundary (*e.g.*, see the recent numerical-experimental correlations [18, 19]), but do not accurately represent peak stress levels on the built-up (detailed) structure. On the other hand, a built-up finite element model (FEM) can more accurately resolve stresses in complex wing constructions, but it is impractical for geometrically nonlinear flutter analysis due to high computational costs and potential convergence issues.

The PROTEUS framework of Werter and De Breuker [12] attempts to address this discrepancy by computing the stiffness and inertia properties of the beam model from an approximation of the three-dimensional (3D) wingbox geometry. The wing is assumed to have a constant cross-section over each beam element, and the beam properties are derived from a cross-sectional analysis tool based on the composite lamination parameters and thicknesses of the skins and spars of the wingbox. The same cross-sectional analysis tool is used to convert strains in the beam model to a more accurate cross-sectional strain distribution used for computing failure criteria. However, to date, no optimization framework has integrated both a built-up FEM of an arbitrary wingbox geometry and a beam model, which enables evaluating all functions of interest with the accuracy, computational cost, and robustness suitable for optimization.

This paper presents a framework that addresses these issues by integrating a geometrically nonlinear flutter constraint into a high-fidelity gradient-based wing structural optimization. The framework optimizes the structural sizing of an arbitrary built-up FEM, which provides the mass objective function along with the linear stress and adjacency constraints. The geometrically nonlinear flutter constraint is computed using a low-order beam representation condensed from the built-up FEM at each optimization step. Thus, a geometrically nonlinear flutter computation constrains the detailed wing structural sizing, without any preset cross-section parametrization, enabling non-homogeneous cross-sectional geometries and material properties. This new contribution sets the present work apart from previous geometrically nonlinear flutter-constrained optimizations [12, 15–17]. The flutter constraint is an aggregate of the damping values for a set of aeroelastic modes and flight conditions [20]. The damping values at each flight condition come from an eigenvalue analysis of the full-order aeroelastic system in a time-domain state-space form, linearized about the wing's geometrically nonlinear statically deformed shape. Thus, the flutter constraint captures geometrically nonlinear effects due to wing's in-flight deflections and their impact on the structural and aerodynamic characteristics. The flutter constraint derivatives with respect to the built-up FEM structural sizing variables are obtained using the adjoint method to enable large-scale gradient-based optimizations [21, Sec. 6.7]. The methodology is demonstrated by optimizing the detailed structural sizing of a high-aspect-ratio rectangular wingbox for minimum weight.

The new contributions from this work are: (1) the integration of consistent built-up FEM and beam models of a wing within gradient-based structural optimization for evaluating the wing mass and stress constraints (built-up FEM) together with a geometrically nonlinear flutter constraint (beam model); (2) the adjoint derivatives of the built-up FEM condensation to a beam and geometrically nonlinear flutter analysis process, enabling gradient-based optimizations with many design variables; (3) the demonstration of the methodology by optimizing the structural sizing of a built-up wingbox model, investigating how geometrically nonlinear effects due to in-flight deflections impact the optimized design. These new contributions are steps toward making gradient-based optimization an effective tool for designing lightweight, high-aspect-ratio wings for highly-energy-efficient aircraft.

The paper is organized as follows: Sec. 2 presents the mathematical formulation of the geometrically nonlinear flutter constraint and its adjoint derivatives with respect to the built-up FEM structural sizing variables; Sec. 3 describes the computational framework; Sec. 4 presents the demonstration case; Sec. 5 discusses the optimization results; the final section presents the conclusions.

2 Geometrically Nonlinear Flutter Constraint

This section formulates the geometrically nonlinear flutter constraint (Sec. 2.1) and its adjoint derivatives with respect to the built-up FEM structural sizing variables (Sec. 2.2). Previous optimizations that included a flutter constraint either considered detailed models but neglected geometrically nonlinear effects (see the review in [8]) or considered geometrically nonlinear effects but evaluated all the functions of interest in a beam model [15–17], in some cases based on an approximate 3D wingbox parametrization [12]. Here, the wing mass objective function and the stress constraints are evaluated using a linear built-up FEM to capture realistic structural features.

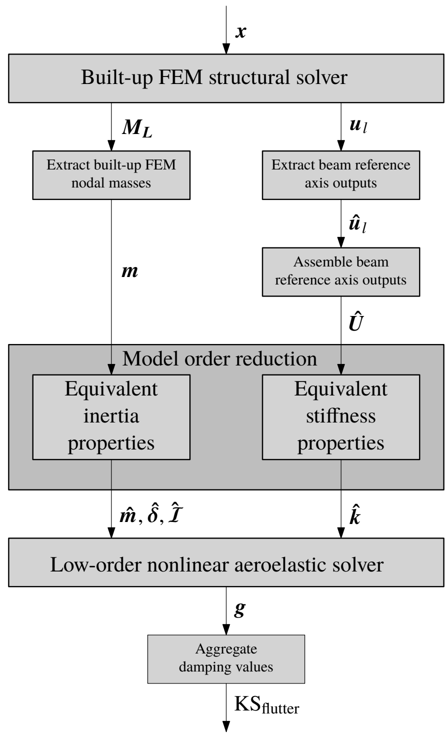

Figure 1: Geometrically nonlinear flutter constraint evaluation process.

The flutter constraint is evaluated using a low-order beam representation derived from the built-up FEM at each optimization step, which makes geometrically nonlinear flutter analyses tractable for optimization. This section presents the methodology, while Sec. 3 describes the computational implementation developed in this work.

2.1 Function Evaluation

Figure 1 shows the process for evaluating the geometrically nonlinear flutter constraint within a high-fidelity gradient-based wing structural optimization. The process considers N_x structural design variables listed in the vector $\boldsymbol{x} \in \mathbb{R}^{N_x}$, which are inputs to the built-up FEM structural solver.

The built-up (detailed) FEM at a given optimization step is condensed to a low-order beam representation for evaluating the geometrically nonlinear flutter constraint. This consists of computing equivalent inertia and stiffness distributions along a user-specified reference axis along the built-up FEM (Fig. 1). The user-specified reference axis is fixed in the optimization and defines the beam model representing the built-up FEM. The beam theory used in this work is the geometrically exact strain-based formulation of Su and Cesnik [22], which uses constant-strain finite elements with extension, twist, and bending curvature in two directions (in-plane and out-of-plane) as the independent structural degrees of freedom (DOFs). However, the methodology can be adapted to other geometrically exact beam theories. In the theory of Su and Cesnik [22], the equivalent inertia distributions associated with the user-specified reference axis consist of constitutive properties that relate the beam generalized forces to the corresponding generalized velocities. Similarly, the equivalent stiffness distributions consist of constitutive properties that relate the beam generalized forces to the generalized strains. The process for obtaining these equivalent beam distributions from a general built-up FEM is described now.

The built-up FEM is discretized in N nodes with body-frame coordinates listed in the vector $\boldsymbol{p} \in \mathbb{R}^{3N}$:

$$\mathbf{p} = \{p_{1_x}, \ldots, p_{N_x}, p_{1_y}, \ldots, p_{N_y}, p_{1_z}, \ldots, p_{N_z}\}^T \tag{1}$$

The inertia distribution of the built-up FEM is described by its consistent mass matrix $\boldsymbol{M} = \boldsymbol{M}(\boldsymbol{x}) \in \mathbb{R}^{6N \times 6N}$ which depends on the design variables $\boldsymbol{x}$. To condense these properties to the beam model, a set of nodal masses is required:

$$\mathbf{m} = \{m_1, \ldots, m_N\}^T \tag{2}$$

The masses in Eq. (2) are obtained by first converting the consistent mass matrix, $\boldsymbol{M}$, to a lumped mass matrix, $\boldsymbol{M}_L$, using the Hinton-Rock-Zienkiewicz (HRZ) method [23]. This lumping process produces a diagonal mass matrix and represents the mass of the structure as a set of uncoupled point masses at the built-up FEM nodes. The masses in Eq. (2) are obtained as the first diagonal value for the translational DOFs in the 6×6 lumped mass matrix block associated with each built-up FEM node. Each 6×6 lumped mass matrix block also contains I_{xx}, I_{yy}, and I_{zz} inertias associated with each shell element node, which have an insignificant effect on the beam inertia properties and are thus discarded in this work.

This lumped-mass approach, however, is unsuitable for rigid-body elements (akin to MSC Nastran CONM2 elements) whose centers of mass are significantly offset from the built-up FEM nodes they are associated with. In these cases, the coupling between the translational and rotational DOFs, which is discarded when the mass matrix is diagonalized, is not negligible. These elements are thus treated separately. For each built-up FEM node associated with a rigid-body element, values are computed for the mass of the rigid body, m_i, its offset from the built-up FEM node, $\boldsymbol{\delta}_i$, and the inertia tensor, $\boldsymbol{\mathcal{I}}_i$ about the point $\boldsymbol{p}_i + \boldsymbol{\delta}_i$. These values are held constant throughout any optimization because, in this work, rigid-body elements are only used to represent non-structural mass distributions that are not optimized.

The offset components are listed in the vector $\boldsymbol{\delta} \in \mathbb{R}^{3N}$:

$$\boldsymbol{\delta} = \{\delta_{1_x}, \ldots, \delta_{N_x}, \delta_{1_y}, \ldots, \delta_{N_y}, \delta_{1_z}, \ldots, \delta_{N_z}\}^T \tag{3}$$

and the inertia tensor components are listed in the vector $\boldsymbol{\mathcal{I}} \in \mathbb{R}^{6N}$:

$$\boldsymbol{\mathcal{I}} = \{\mathcal{I}_{1_{xx}}, \ldots, \mathcal{I}_{N_{xx}}, \mathcal{I}_{1_{yy}}, \ldots, \mathcal{I}_{N_{yy}}, \mathcal{I}_{1_{zz}}, \ldots, \mathcal{I}_{N_{zz}}, \mathcal{I}_{1_{xy}}, \ldots, \mathcal{I}_{N_{xy}}, \mathcal{I}_{1_{xz}}, \ldots, \mathcal{I}_{N_{xz}}, \mathcal{I}_{1_{yz}}, \ldots, \mathcal{I}_{N_{yz}}\}^T \tag{4}$$

The beam model is represented by a user-specified reference axis, discretized in $\hat{N}$ nodes. The body-frame coordinates of these nodes are listed in the vector $\hat{\boldsymbol{p}} \in \mathbb{R}^{3\hat{N}}$:

$$\hat{\mathbf{p}} = \{\hat{p}_{1_x}, \ldots, \hat{p}_{\hat{N}_x}, \hat{p}_{1_y}, \ldots, \hat{p}_{\hat{N}_y}, \hat{p}_{1_z}, \ldots, \hat{p}_{\hat{N}_z}\}^T \tag{5}$$

The equivalent inertia distribution of the beam is given by a set of $\hat{N}$ rigid-body elements associated with the reference axis nodes. Each rigid-body element is described by its mass, its center-of-mass offset from the corresponding beam reference axis node, and an inertia tensor about its center of mass, which results in a concentrated-parameters beam mass model. In this work, "equivalent inertia distributions" means the spanwise distributions of the rigid-body masses, center-of-mass offset, and inertia tensor components, instead of the elements of a cross-sectional mass matrix (distributed-mass model). The mass values of the rigid-body elements associated with the reference axis nodes are listed in the vector $\hat{\boldsymbol{m}} \in \mathbb{R}^{\hat{N}}$:

$$\hat{\mathbf{m}} = \{\hat{m}_1, \ldots, \hat{m}_{\hat{N}}\}^T \tag{6}$$

The offsets of the rigid-body element's center of mass from the corresponding beam reference axis node are listed in the vector $\hat{\boldsymbol{\delta}} \in \mathbb{R}^{3\hat{N}}$:

$$\hat{\boldsymbol{\delta}} = \{\hat{\delta}_{1_x}, \dots, \hat{\delta}_{\hat{N}_x}, \hat{\delta}_{1_y}, \dots, \hat{\delta}_{\hat{N}_y}, \hat{\delta}_{1_z}, \dots, \hat{\delta}_{\hat{N}_z}\}^T \tag{7}$$

The inertia tensor components about the points $\hat{\boldsymbol{p}} + \hat{\boldsymbol{\delta}}$ are listed in the vector $\hat{\boldsymbol{\mathcal{I}}} \in \mathbb{R}^{6\hat{N}}$:

$$\hat{\boldsymbol{\mathcal{I}}} = \{\hat{\mathcal{I}}_{1_{xx}}, \dots, \hat{\mathcal{I}}_{\hat{N}_{xx}}, \hat{\mathcal{I}}_{1_{yy}}, \dots, \hat{\mathcal{I}}_{\hat{N}_{yy}}, \hat{\mathcal{I}}_{1_{zz}}, \dots, \hat{\mathcal{I}}_{\hat{N}_{zz}}, \hat{\mathcal{I}}_{1_{xy}}, \dots, \hat{\mathcal{I}}_{\hat{N}_{xy}}, \hat{\mathcal{I}}_{1_{xz}}, \dots, \hat{\mathcal{I}}_{\hat{N}_{xz}}, \hat{\mathcal{I}}_{1_{yz}}, \dots, \hat{\mathcal{I}}_{\hat{N}_{yz}}\}^T \tag{8}$$

The masses $\hat{\boldsymbol{m}}$, center-of-mass offsets $\hat{\boldsymbol{\delta}}$, and inertia tensors $\hat{\boldsymbol{\mathcal{I}}}$ in Eqs. (6), (7), and (8) depend on the built-up FEM mass matrix through the nodal masses $\boldsymbol{m}$ in Eq. (2), that is, $\hat{\mathbf{m}} = \hat{\mathbf{m}}(\mathbf{m})$, $\hat{\boldsymbol{\delta}} = \hat{\boldsymbol{\delta}}(\mathbf{m})$, and $\hat{\boldsymbol{\mathcal{I}}} = \hat{\boldsymbol{\mathcal{I}}}(\mathbf{m})$. These quantities also depend on the offsets and inertia tensors provided by the built-up FEM mass matrix, given in Eqs. (3) and (4), if nonzero, as is the case where rigid-body elements are present that have center of mass offsets or moments of inertia associated with them, or both. This dependency is omitted here because the center-of-mass offsets and inertia tensors associated with the rigid-body elements remain constant during optimization in this work. However, this dependency may be included in a general case where the built-up FEM includes rigid-body elements with non-zero center of mass offsets or moments of inertia that are updated within the optimization. The quantities $\hat{\boldsymbol{m}}, \hat{\boldsymbol{\delta}}, \hat{\boldsymbol{\mathcal{I}}}$ in Eqs. (6), (7), and (8) provide the equivalent inertia distribution of the beam model representing the built-up FEM, used to evaluate the geometrically nonlinear flutter constraint.

In this work, "equivalent stiffness distributions" means the spanwise distributions of the entries of the 4×4 cross-sectional stiffness matrix of the geometrically exact, strain-based beam formulation of Su and Cesnik [22]. This cross-sectional stiffness matrix is associated with the Euler-Bernoulli-like formulation for non-isotropic beams and is related to the 6×6 Timoshenko-like cross-sectional stiffness matrix by eliminating the transverse shear effects through an energy minimization process [24]. In this work, the cross-sectional stiffness matrices needed for the flutter analysis must come directly from the built-up FEM through a numerical identification process. This process enables the extraction of the cross-sectional stiffness constants, not only for uniform prismatic structures, but for built-up FEM of arbitrary complexity, which is required when dealing with general wingbox configurations. The identified equivalent stiffness distributions are given in the vector $\hat{\boldsymbol{k}} \in \mathbb{R}^{10\hat{M}}$ defined in Eq. (9), where $\hat{M} = \hat{N} - 1$ is the number of elements defined by pairs of consecutive beam reference axis nodes:

$$\hat{\mathbf{k}} = \{\hat{\mathbf{k}}_{11}^T, \hat{\mathbf{k}}_{22}^T, \hat{\mathbf{k}}_{33}^T, \hat{\mathbf{k}}_{44}^T, \hat{\mathbf{k}}_{12}^T, \hat{\mathbf{k}}_{13}^T, \hat{\mathbf{k}}_{14}^T, \hat{\mathbf{k}}_{23}^T, \hat{\mathbf{k}}_{24}^T, \hat{\mathbf{k}}_{34}^T\}^T \tag{9}$$

$$\begin{aligned}
&\hat{\mathbf{k}}_{11} = \{\hat{k}_{1_{11}}, \dots, \hat{k}_{\hat{M}_{11}}\}^T \quad \hat{\mathbf{k}}_{22} = \{\hat{k}_{1_{22}}, \dots, \hat{k}_{\hat{M}_{22}}\}^T \quad \hat{\mathbf{k}}_{33} = \{\hat{k}_{1_{33}}, \dots, \hat{k}_{\hat{M}_{33}}\}^T \\
&\hat{\mathbf{k}}_{44} = \{\hat{k}_{1_{44}}, \dots, \hat{k}_{\hat{M}_{44}}\}^T \quad \hat{\mathbf{k}}_{12} = \{\hat{k}_{1_{12}}, \dots, \hat{k}_{\hat{M}_{12}}\}^T \quad \hat{\mathbf{k}}_{13} = \{\hat{k}_{1_{13}}, \dots, \hat{k}_{\hat{M}_{13}}\}^T \\
&\hat{\mathbf{k}}_{14} = \{\hat{k}_{1_{14}}, \dots, \hat{k}_{\hat{M}_{14}}\}^T \quad \hat{\mathbf{k}}_{23} = \{\hat{k}_{1_{23}}, \dots, \hat{k}_{\hat{M}_{23}}\}^T \quad \hat{\mathbf{k}}_{24} = \{\hat{k}_{1_{24}}, \dots, \hat{k}_{\hat{M}_{24}}\}^T \\
&\hat{\mathbf{k}}_{34} = \{\hat{k}_{1_{34}}, \dots, \hat{k}_{\hat{M}_{34}}\}^T
\end{aligned} \tag{10}$$

The quantities in Eqs. (9) and (10) are the constants of the 4×4 cross-sectional stiffness matrices according to the geometrically exact strain-based beam formulation of Su and Cesnik [22]. These constants depend on the assembled displacement outputs (translations and rotations) of the beam reference axis nodes for six independent static loads applied to the built-up FEM, $\hat{\boldsymbol{k}} = \hat{\boldsymbol{k}}(\hat{\boldsymbol{U}})$.

The assembled displacement output vector $\hat{\boldsymbol{U}} \in \mathbb{R}^{36\hat{N}}$ is obtained as follows. The built-up FEM displacement vector for a generic load case, $\boldsymbol{u} = \boldsymbol{u}(\boldsymbol{x}) \in \mathbb{R}^{6N}$, depends implicitly on the design variables $\boldsymbol{x}$ through the solution of a linear static structural analysis. The displacement vector for the lth load case used for stiffness identification is denoted by $\boldsymbol{u}_l$, that is, $\boldsymbol{u}_1 \ldots \boldsymbol{u}_l \ldots \boldsymbol{u}_6$ are the displacement vectors for the six independent load cases: three tip forces and three tip moments. The stiffness identification does not require the displacements of the entire built-up FEM but only of the beam reference axis nodes, which are recovered via interpolation elements. These interpolation elements are akin to MSC Nastran RBE3 elements (though this work uses a different finite element solver, see Sec. 3). The displacement outputs at the beam reference axis nodes are extracted from the full displacement output $\boldsymbol{u}_l$ for the lth load case using a search process and are stacked into $\hat{\boldsymbol{u}}_l$. This process is written as $\hat{\boldsymbol{u}}_l = \hat{\boldsymbol{u}}_l(\boldsymbol{u}_l) \in \mathbb{R}^{6\hat{N}}$ and gives

$$\hat{\boldsymbol{u}}_l = \{\hat{u}_{l,11}, \ldots, \hat{u}_{l,16}, \ldots, \hat{u}_{l,j1}, \ldots, \hat{u}_{l,j6}, \ldots, \hat{u}_{l,\hat{N}1}, \ldots, \hat{u}_{l,\hat{N}6}\}^T \tag{11}$$

where $\hat{u}_{l,j1}$ is the displacement output for the first DOF of the jth beam reference axis node for the lth load case. The linear static displacements (translations and rotations) of the beam reference axis nodes for the six independent load cases are assembled into the output vector

$$\hat{\boldsymbol{U}} = \hat{\boldsymbol{U}}(\hat{\boldsymbol{u}}_1, \hat{\boldsymbol{u}}_2, \hat{\boldsymbol{u}}_3, \hat{\boldsymbol{u}}_4, \hat{\boldsymbol{u}}_5, \hat{\boldsymbol{u}}_6) \tag{12}$$

This vector is built by extracting the kth displacement output for the jth reference axis node and lth load case, given by $\hat{u}_{l,jk}$, such that

$$\begin{aligned}
\hat{\boldsymbol{U}} = \{&\hat{u}_{1,11}, \ldots, \hat{u}_{1,16}, \ldots, \hat{u}_{l,11} \ldots, \hat{u}_{l,16}, \ldots, \hat{u}_{6,11}, \ldots, \hat{u}_{6,16}, \\
&\hat{u}_{1,21}, \ldots, \hat{u}_{1,26}, \ldots, \hat{u}_{l,21} \ldots, \hat{u}_{l,26}, \ldots, \hat{u}_{6,21}, \ldots, \hat{u}_{6,26}, \\
&\ldots, \\
&\hat{u}_{1,j1}, \ldots, \hat{u}_{1,j6}, \ldots, \hat{u}_{l,j1} \ldots, \hat{u}_{l,j6}, \ldots, \hat{u}_{6,j1}, \ldots, \hat{u}_{6,j6}, \\
&\ldots, \\
&\hat{u}_{1,\hat{N}1}, \ldots, \hat{u}_{1,\hat{N}6}, \ldots, \hat{u}_{l,\hat{N}1} \ldots, \hat{u}_{l,\hat{N}6}, \ldots, \hat{u}_{6,\hat{N}1}, \ldots, \hat{u}_{6,\hat{N}6}\}^T
\end{aligned} \tag{13}$$

The assembled displacement vector in Eq. (13) is used to compute the equivalent stiffness distributions of the beam model [25, 26] (that is, the spanwise distributions of the constants of the cross-sectional stiffness matrix). This provides the 10 independent stiffness constants for each beam element based on the differential displacements of its ends. While each displacement-based FEM node is associated with six DOFs, three translations and three rotations, each strain-based beam element is described by the entries of a symmetric 4×4 matrix, resulting in 10 distinct stiffness constants. This is because the strain-based beam formulation of Su and Cesnik [22] assumes finite elements with four independent DOFs (Euler-Bernoulli-like formulation). The shear DOFs are eliminated by condensing their effects through energy minimization [24], leading to the 4×4 cross-sectional constitutive law given in Eqs. (9) and (10).

The equivalent inertia and stiffness distributions detailed above define the low-order beam representation of the built-up FEM at a given optimization step. In this work, the beam model is coupled to the potential flow unsteady thin airfoil theory of Peters *et al.* [27] to obtain the aeroelastic model for the geometrically nonlinear flutter analysis. This aerodynamic formulation is a popular choice for flutter analysis of geometrically nonlinear wings operating at low speeds [3, 6, 28]. Since the focus of this study is on the impact of geometrically nonlinear effects on high-fidelity gradient-based structural optimization, this formulation is adequate. Considering aerodynamic nonlinearities due to, for instance, transonic effects is beyond the scope of the present work and would require a different aerodynamic model.

The geometrically nonlinear flutter constraint builds on the linear damping-based formulation of Jonsson et al. [20] and its extension to capture geometrically nonlinear effects [17]. Consider a nonlinear aeroelastic system governed by

$$\dot{\boldsymbol{y}} = \boldsymbol{f}(\boldsymbol{y}(\boldsymbol{c},\boldsymbol{x}),\boldsymbol{c},\boldsymbol{x}) \tag{14}$$

where $\boldsymbol{y}$ is the $N_y \times 1$ state vector and $\boldsymbol{c}$ is the $N_c \times 1$ vector of control parameters. These parameters identify a point in the flight envelope in terms of boundary conditions (*e.g.*, load factor or angle of attack) and flight conditions (*e.g.*, Mach number and altitude or dynamic pressure).

The stability of the nonlinear aeroelastic system, Eq. (14), for a given design $\boldsymbol{x}$ is assessed at N_s flight envelope points $\boldsymbol{c}_i$ of interest for the stability (flutter) analysis ($i = 1,\ldots,N_s$). Each flight envelope point $\boldsymbol{c}_i$ is associated with an equilibrium state $\boldsymbol{y}_{e_i}(\boldsymbol{x}) := \boldsymbol{y}_e(\boldsymbol{c}_i,\boldsymbol{x})$ that satisfies

$$\boldsymbol{f}(\boldsymbol{y}_{e_i}(\boldsymbol{x}),\boldsymbol{c}_i,\boldsymbol{x}) = \boldsymbol{0} \tag{15}$$

The small-amplitude dynamics about the nonlinear equilibrium state $\boldsymbol{y}_{e_i}(\mathbf{x})$ is governed by state-space linearized equations

$$\Delta\dot{\boldsymbol{y}} = \boldsymbol{A}_i\,\Delta\boldsymbol{y} \tag{16}$$

where $\Delta\boldsymbol{y} := \boldsymbol{y} - \boldsymbol{y}_{e_i}$ is the $N \times 1$ state perturbation vector and

$$\boldsymbol{A}_i := \boldsymbol{A}_i(\boldsymbol{x}) = \frac{\partial \boldsymbol{f}(\boldsymbol{y}(\boldsymbol{c},\boldsymbol{x}),\boldsymbol{c},\boldsymbol{x})}{\partial \boldsymbol{y}}\bigg|_{\boldsymbol{y}(\boldsymbol{c},\boldsymbol{x})=\boldsymbol{y}_{e_i}(\boldsymbol{x}),\,\boldsymbol{c}=\boldsymbol{c}_i} \tag{17}$$

is the $N_y \times N_y$ Jacobian matrix of the system (14) with respect to the state vector $\boldsymbol{y}$ at the equilibrium state $\boldsymbol{y}_{e_i}$, also known as the state matrix. The stability of the system about $\boldsymbol{y}_{e_i}$ is determined by an eigenvalue analysis. Defining $\Delta\boldsymbol{y}_{ik} = \Delta\bar{\boldsymbol{y}}_{ik}e^{\sigma_{ik}t}$ and inserting in Eq. (16) gives the standard eigenvalue problem

$$\sigma_{ik}\Delta\bar{\boldsymbol{y}}_{ik} = \boldsymbol{A}_i\Delta\bar{\boldsymbol{y}}_{ik} \tag{18}$$

The eigenvalues of $\boldsymbol{A}_i(\boldsymbol{x})$ are denoted by $\sigma_{ik}(\boldsymbol{x}) := g_{ik}(\boldsymbol{x}) + j\omega_{ik}(\boldsymbol{x})$ ($k = 1,\ldots,N_y$), where $g_{ik}(\boldsymbol{x})$ is the damping associated with the kth mode at the ith equilibrium state, $\omega_{ik}(\boldsymbol{x})$ the corresponding angular frequency, and j the imaginary unit. The eigenvectors, $\Delta\bar{\boldsymbol{y}}_{ik}(\boldsymbol{x})$, of $\boldsymbol{A}_i(\boldsymbol{x})$ associated with the eigenvalues $\sigma_{ik}(\boldsymbol{x})$ are the aeroelastic mode shapes of the linearized aeroelastic system about the nonlinear equilibrium state $\boldsymbol{y}_{e_i}(\boldsymbol{x})$, *i.e.*, accounting for the statically deformed shape. Note that, in this work, the aeroelastic system linearized about each nonlinear equilibrium state is described by a time-domain state-space model, according to Eq. (16). Thus, eigenvalues of $\boldsymbol{A}_i(\boldsymbol{x})$ are computed using standard eigenvalue analyses techniques instead of, for instance, the p–k method. However, the methodology presented in this work can also be applied to cases where the aeroelastic system is not cast in time-domain state-space form, as in the case of frequency-domain unsteady aerodynamic models. The methodology is agnostic to the method used to compute the aeroelastic eigenvalues.

The equilibrium state $\boldsymbol{y}_{e_i}(\boldsymbol{x})$ associated with the ith flight envelope point $\boldsymbol{c}_i$ is stable (that is, no flutter occurs) if the damping values $g_{ik}(\boldsymbol{x})$ are all negative. This aeroelastic stability requirement translates to the damping-based flutter constraints

$$g'_{ik}(\boldsymbol{x}) := g_{ik}(\boldsymbol{x}) - G_i \leq 0 \qquad \begin{array}{l}\forall\, i = 1,\ldots,N_s\\ \forall\, k = 1,\ldots,N_m\end{array} \tag{19}$$

where $N_m \leq N_y$ is the number of modes whose eigenvalues are used in the constraint, which may be lower than the DOFs in Eq. (16). The quantity $G_i = G(\boldsymbol{c}_i)$ in Eq. (19) is the value of a damping bounding curve at the flight envelope point $\boldsymbol{c}_i$. The bounding curve can serve multiple purposes.

For example, a negative value forces a more robust design by requiring a residual damping margin when the flutter constraint is active [20]. Alternatively, a positive value of the damping curve avoids constraint violations due to marginally stable modes that are not of practical concern because, in reality, they would be stabilized by unmodeled damping sources.

The constraints given in Eq. (19) are suitable for gradient-based optimization because they are continuous, smooth, and differentiable functions of the design variables [8]. However, their large number $N_s \times N_m$ makes computing derivatives infeasible in practical problems with many design variables. Thus, Eq. (19) is reduced to a scalar metric using the Kreisselmeier–Steinhauser (KS) aggregation function [29–31]. The aggregation enables computing derivatives efficiently using adjoint methods that scale with the number of outputs (objective function and constraints) but are independent of the number of design variables [21, Sec. 6.7].

Assuming a constraint value of the aggregation parameter ρ_{KS} for all the damping values gives

$$\text{KS}_{\text{flutter}}(\boldsymbol{x}) := g'_{\max}(\boldsymbol{x}) + \frac{1}{\rho_{\text{KS}}} \ln \left\{ \sum_{i=1}^{N_s} \sum_{k=1}^{N_m} \exp \left\{ \rho_{\text{KS}} \left[g'_{ik}(\boldsymbol{x}) - g'_{\max}(\boldsymbol{x}) \right] \right\} \right\} \leq 0 \tag{20}$$

This scalar flutter constraint is a conservative estimate of the most positive bounded damping value in Eq. (19), denoted by $g'_{\max}(\boldsymbol{x})$, and tends to that quantity as the aggregation parameter tends to infinity [21, Sec. 5.7]. The aggregated KS constraint in Eq. (20) needs to be less than or equal to zero for the design to be feasible, and a value of zero means the constraint is active.

The flutter constraint in Eq. (20) captures geometrically nonlinear effects associated with in-flight deflections, which are neglected in linear flutter analyses based on the wing undeformed shape [2]. Because flutter occurs when a complex-conjugate eigenvalue of the system linearized about a nonlinear equilibrium [Eq. (16)] achieves a positive real part, a sequence of linearized analyses about nonlinear equilibrium states can provide the stability characteristics of the system [6].

2.2 Adjoint Derivatives

The geometrically nonlinear flutter constraint dependency on the design variables associated with the built-up FEM structural sizing can be represented as

$$\begin{aligned}\text{KS}_{\text{flutter}}(\boldsymbol{x}) &= \text{KS}(\boldsymbol{g}'(\hat{\boldsymbol{k}}, \hat{\boldsymbol{m}}, \hat{\boldsymbol{\delta}}, \hat{\boldsymbol{\mathcal{I}}})) \\ &= \text{KS}(\boldsymbol{g}'(\hat{\boldsymbol{k}}(\hat{\boldsymbol{U}}(\hat{\boldsymbol{u}}_1(\boldsymbol{u_1}(\boldsymbol{x})), \ldots, \hat{\boldsymbol{u}}_6(\boldsymbol{u_6}(\boldsymbol{x})))), \hat{\boldsymbol{m}}(\boldsymbol{m}(\boldsymbol{M}(\boldsymbol{x}))), \hat{\boldsymbol{\delta}}(\boldsymbol{m}(\boldsymbol{M}(\boldsymbol{x}))), \hat{\boldsymbol{\mathcal{I}}}(\boldsymbol{m}(\boldsymbol{M}(\boldsymbol{x})))))\end{aligned} \tag{21}$$

Since the stiffness condensation relies on the solution of six large systems of equations (the static structural analyses), derivatives of the flutter constraint must be computed using the adjoint method, which is described below.

2.2.1 Derivative Definitions

The functions of interest are listed in the $N_f \times 1$ vector $\boldsymbol{\mathcal{F}}$. For a given set of control parameters $\boldsymbol{c} = \boldsymbol{c}_i$, these functions depend on the design variables $\boldsymbol{x}$ and on the state variables of the system $\boldsymbol{y}(\boldsymbol{x})$, which depend implicitly on the design variables:

$$\boldsymbol{\mathcal{F}} = \boldsymbol{\mathcal{F}}(\boldsymbol{x}, \boldsymbol{y}(\boldsymbol{x})) \tag{22}$$

where the residual equation is

$$\boldsymbol{R} = \boldsymbol{R}(\boldsymbol{x}, \boldsymbol{y}(\boldsymbol{x})) = \boldsymbol{0} \tag{23}$$

The total derivative of the functions of interest is

$$\frac{d\boldsymbol{\mathcal{F}}}{d\boldsymbol{x}} = \frac{\partial \boldsymbol{\mathcal{F}}}{\partial \boldsymbol{x}} + \frac{\partial \boldsymbol{\mathcal{F}}}{\partial \boldsymbol{y}} \frac{d\boldsymbol{y}}{d\boldsymbol{x}} \tag{24}$$

and the total derivative of the residual equation is

$$\frac{d\boldsymbol{R}}{d\boldsymbol{x}} = \frac{\partial \boldsymbol{R}}{\partial \boldsymbol{x}} + \frac{\partial \boldsymbol{R}}{\partial \boldsymbol{y}} \frac{d\boldsymbol{y}}{d\boldsymbol{x}} = \boldsymbol{0} \tag{25}$$

Rearranging Eq. (25) yields

$$\frac{\partial \boldsymbol{R}}{\partial \boldsymbol{y}} \frac{d\boldsymbol{y}}{d\boldsymbol{x}} = -\frac{\partial \boldsymbol{R}}{\partial \boldsymbol{x}} \tag{26}$$

$$\frac{d\boldsymbol{y}}{d\boldsymbol{x}} = -\left[\frac{\partial \boldsymbol{R}}{\partial \boldsymbol{y}}\right]^{-1} \frac{\partial \boldsymbol{R}}{\partial \boldsymbol{x}} \tag{27}$$

and combining this relation with Eq. (24) yields

$$\frac{d\boldsymbol{\mathcal{F}}}{d\boldsymbol{x}} = \frac{\partial \boldsymbol{\mathcal{F}}}{\partial \boldsymbol{x}} - \frac{\partial \boldsymbol{\mathcal{F}}}{\partial \boldsymbol{y}} \left[\frac{\partial \boldsymbol{R}}{\partial \boldsymbol{y}}\right]^{-1} \frac{\partial \boldsymbol{R}}{\partial \boldsymbol{x}} \tag{28}$$

This total derivative can be computed using the *direct* or *adjoint* method. The adjoint equations are written as

$$\left[\frac{\partial \boldsymbol{R}}{\partial \boldsymbol{y}}\right]^{T} \boldsymbol{\psi} = \left[\frac{\partial \boldsymbol{\mathcal{F}}}{\partial \boldsymbol{y}}\right]^{T} \tag{29}$$

where $\boldsymbol{\psi}$ is the $N_x \times N_f$ adjoint matrix. The ith column is the adjoint vector $\boldsymbol{\psi}_i$ from a linear solve with a right-hand side of $[\partial \mathcal{F}_i / \partial \boldsymbol{y}]^T$ for the ith function of interest. Computing the adjoint matrix requires N_f linear solves. Next, substituting into Eq. (28) yields

$$\frac{d\boldsymbol{\mathcal{F}}}{d\boldsymbol{x}} = \frac{\partial \boldsymbol{\mathcal{F}}}{\partial \boldsymbol{x}} - \boldsymbol{\psi}^T \frac{\partial \boldsymbol{R}}{\partial \boldsymbol{x}} \tag{30}$$

Alternatively, one can use the direct method

$$\frac{\partial \boldsymbol{R}}{\partial \boldsymbol{y}} \frac{d\boldsymbol{y}}{d\boldsymbol{x}} = \frac{\partial \boldsymbol{R}}{\partial \boldsymbol{x}} \tag{31}$$

$$\frac{\partial \boldsymbol{R}}{\partial \boldsymbol{y}} \boldsymbol{\phi} = \frac{\partial \boldsymbol{R}}{\partial \boldsymbol{x}} \tag{32}$$

This linear system needs to be solved N_x times to get the full $d\boldsymbol{y}/d\boldsymbol{x}$. The ith column is the direct vector $\boldsymbol{\phi}_i$ from a linear solve with a right-hand side of $[\partial \boldsymbol{R} / \partial x_i]$ for the ith design variable. Once the entire matrix $\boldsymbol{\phi}$ is known, one obtains

$$\frac{d\boldsymbol{\mathcal{F}}}{d\boldsymbol{x}} = \frac{\partial \boldsymbol{\mathcal{F}}}{\partial \boldsymbol{x}} - \frac{\partial \boldsymbol{R}}{\partial \boldsymbol{x}} \boldsymbol{\phi} \tag{33}$$

In this work, the total derivatives of the geometrically nonlinear flutter constraint with respect to the built-up FEM design variables are computed using the adjoint method. This enables large-scale gradient-based optimizations with many design variables but few outputs of interest (objective function and constraints). The adjoint method is the most suitable for these problems because it does not scale with the number of design variables. The derivation below assumes that the derivatives associated with all blocks in Fig. 1 are known and the derivative $\partial \mathrm{KS}_{\text{flutter}}/\partial \boldsymbol{u}_l$ for the lth load case exists. One can use the adjoint equation (29) by substituting the lth derivative in for the right-hand side and by solving the linear system:

$$\left[\frac{\partial \boldsymbol{R}_l}{\partial \boldsymbol{u}_l}\right]^T \boldsymbol{\psi}_l = \left[\frac{\partial \mathrm{KS}_{\text{flutter}}}{\partial \boldsymbol{u}_l}\right]^T \tag{34}$$

This linear system needs to be solved for six load cases associated with the linear static solutions used in the equivalent stiffness identification. Next, the total derivative of the flutter constraint with respect to the build-up FEM structural sizing variables is

$$\frac{d\mathrm{KS}_{\text{flutter}}}{d\boldsymbol{x}} = \frac{\partial \mathrm{KS}_{\text{flutter}}}{\partial \boldsymbol{x}} - \sum_{l=1}^{6} \left(\boldsymbol{\psi}_l^T \frac{\partial \boldsymbol{R}_l}{\partial \boldsymbol{x}} \right) \tag{35}$$

The derivation of each term necessary for computing Eq. (34) and (35) is reported below.

2.2.2 Computing $\partial \mathrm{KS}_{\text{flutter}}/\partial x$

To compute $\partial \mathrm{KS}_{\text{flutter}}/\partial \boldsymbol{x}$, one needs to vary the design variables while keeping the state variables (displacement outputs of the linear static solutions) fixed and re-evaluate the geometrically nonlinear flutter constraint. The partial derivative chain is given by

$$\begin{aligned} \frac{\partial \mathrm{KS}_{\text{flutter}}}{\partial \boldsymbol{x}} &= \frac{\partial \mathrm{KS}_{\text{flutter}}}{\partial \boldsymbol{g}} \frac{\partial \boldsymbol{g}}{\partial \hat{\boldsymbol{k}}} \frac{\partial \hat{\boldsymbol{k}}}{\partial \hat{\boldsymbol{U}}} \frac{\partial \hat{\boldsymbol{U}}}{\partial \boldsymbol{x}} + \frac{\partial \mathrm{KS}_{\text{flutter}}}{\partial \boldsymbol{g}} \left(\frac{\partial \boldsymbol{g}}{\partial \hat{\boldsymbol{m}}} \frac{\partial \hat{\boldsymbol{m}}}{\partial \boldsymbol{m}} + \frac{\partial \boldsymbol{g}}{\partial \hat{\boldsymbol{\delta}}} \frac{\partial \hat{\boldsymbol{\delta}}}{\partial \boldsymbol{m}} + \frac{\partial \boldsymbol{g}}{\partial \hat{\boldsymbol{\mathcal{I}}}} \frac{\partial \hat{\boldsymbol{\mathcal{I}}}}{\partial \boldsymbol{m}} \right) \frac{\partial \boldsymbol{m}}{\partial \boldsymbol{M}_L} \frac{\partial \boldsymbol{M}_L}{\partial \boldsymbol{x}} && (36) \\ &= \frac{\partial \mathrm{KS}_{\text{flutter}}}{\partial \boldsymbol{g}} \left(\frac{\partial \boldsymbol{g}}{\partial \hat{\boldsymbol{m}}} \frac{\partial \hat{\boldsymbol{m}}}{\partial \boldsymbol{m}} + \frac{\partial \boldsymbol{g}}{\partial \hat{\boldsymbol{\delta}}} \frac{\partial \hat{\boldsymbol{\delta}}}{\partial \boldsymbol{m}} + \frac{\partial \boldsymbol{g}}{\partial \hat{\boldsymbol{\mathcal{I}}}} \frac{\partial \hat{\boldsymbol{\mathcal{I}}}}{\partial \boldsymbol{m}} \right) \frac{\partial \boldsymbol{m}}{\partial \boldsymbol{M}_L} \frac{\partial \boldsymbol{M}_L}{\partial \boldsymbol{x}} && (37) \end{aligned}$$

The leading term in Equation (36) is removed because the states (displacement outputs from the linear static solution) depend implicitly but not explicitly on the design variables, $\partial \boldsymbol{u}_l/\partial \boldsymbol{x} = \boldsymbol{0}$:

$$\frac{\partial \hat{\boldsymbol{U}}}{\partial \boldsymbol{x}} = \frac{\partial \hat{\boldsymbol{U}}}{\partial \hat{\boldsymbol{u}}_1} \frac{\partial \hat{\boldsymbol{u}}_1}{\partial \boldsymbol{u}_1} \frac{\partial \boldsymbol{u}_1}{\partial \boldsymbol{x}} + \frac{\partial \hat{\boldsymbol{U}}}{\partial \hat{\boldsymbol{u}}_2} \frac{\partial \hat{\boldsymbol{u}}_2}{\partial \boldsymbol{u}_2} \frac{\partial \boldsymbol{u}_2}{\partial \boldsymbol{x}} + \cdots + \frac{\partial \hat{\boldsymbol{U}}}{\partial \hat{\boldsymbol{u}}_6} \frac{\partial \hat{\boldsymbol{u}}_6}{\partial \boldsymbol{u}_6} \frac{\partial \boldsymbol{u}_6}{\partial \boldsymbol{x}} = \sum_{l=1}^{6} \left(\frac{\partial \hat{\boldsymbol{U}}}{\partial \hat{\boldsymbol{u}}_l} \frac{\partial \hat{\boldsymbol{u}}_l}{\partial \boldsymbol{u}_l} \frac{\partial \boldsymbol{u}_l}{\partial \boldsymbol{x}} \right) = \boldsymbol{0} \tag{38}$$

By differentiating Eq. (21) with respect to the displacement outputs for the lth static load case, $\boldsymbol{u}_l$, the partial derivative can be written as

$$\begin{aligned} \frac{\partial \mathrm{KS}_{\text{flutter}}}{\partial \boldsymbol{u}_l} &= \frac{\partial \mathrm{KS}_{\text{flutter}}}{\partial \boldsymbol{g}} \left[\frac{\partial \boldsymbol{g}}{\partial \hat{\boldsymbol{k}}} \frac{\partial \hat{\boldsymbol{k}}}{\partial \hat{\boldsymbol{U}}} \frac{\partial \hat{\boldsymbol{U}}}{\partial \hat{\boldsymbol{u}}_l} \frac{\partial \hat{\boldsymbol{u}}_l}{\partial \boldsymbol{u}_l} + \frac{\partial \boldsymbol{g}}{\partial \hat{\boldsymbol{m}}} \frac{\partial \hat{\boldsymbol{m}}}{\partial \hat{\boldsymbol{U}}} \frac{\partial \hat{\boldsymbol{U}}}{\partial \hat{\boldsymbol{u}}_l} \frac{\partial \hat{\boldsymbol{u}}_l}{\partial \boldsymbol{u}_l} + \frac{\partial \boldsymbol{g}}{\partial \hat{\boldsymbol{\delta}}} \frac{\partial \hat{\boldsymbol{\delta}}}{\partial \hat{\boldsymbol{U}}} \frac{\partial \hat{\boldsymbol{U}}}{\partial \hat{\boldsymbol{u}}_l} \frac{\partial \hat{\boldsymbol{u}}_l}{\partial \boldsymbol{u}_l} + \frac{\partial \boldsymbol{g}}{\partial \hat{\boldsymbol{\mathcal{I}}}} \frac{\partial \hat{\boldsymbol{\mathcal{I}}}}{\partial \hat{\boldsymbol{U}}} \frac{\partial \hat{\boldsymbol{U}}}{\partial \hat{\boldsymbol{u}}_l} \frac{\partial \hat{\boldsymbol{u}}_l}{\partial \boldsymbol{u}_l} \right] && (39) \\ &= \frac{\partial \mathrm{KS}_{\text{flutter}}}{\partial \boldsymbol{g}} \frac{\partial \boldsymbol{g}}{\partial \hat{\boldsymbol{k}}} \frac{\partial \hat{\boldsymbol{k}}}{\partial \hat{\boldsymbol{U}}} \frac{\partial \hat{\boldsymbol{U}}}{\partial \hat{\boldsymbol{u}}_l} \frac{\partial \hat{\boldsymbol{u}}_l}{\partial \boldsymbol{u}_l} && (40) \end{aligned}$$

The terms $\partial \hat{\boldsymbol{m}}/\partial \hat{\boldsymbol{U}} = \partial \hat{\boldsymbol{\delta}}/\partial \hat{\boldsymbol{U}} = \partial \hat{\boldsymbol{\mathcal{I}}}/\partial \hat{\boldsymbol{U}} = \boldsymbol{0}$ because the equivalent inertia distributions are independent of the displacement outputs needed to identify the equivalent stiffness distributions. Rewriting as transpose for adjoint equation of efficient matrix-vector products yields

$$\frac{\partial \mathrm{KS}_{\text{flutter}}}{\partial \boldsymbol{u}_l}^T = \frac{\partial \hat{\boldsymbol{u}}_l}{\partial \boldsymbol{u}_l}^T \frac{\partial \hat{\boldsymbol{U}}}{\partial \hat{\boldsymbol{u}}_l}^T \frac{\partial \hat{\boldsymbol{k}}}{\partial \hat{\boldsymbol{U}}}^T \frac{\partial \boldsymbol{g}}{\partial \hat{\boldsymbol{k}}}^T \frac{\partial \mathrm{KS}_{\text{flutter}}}{\partial \boldsymbol{g}}^T \tag{41}$$

The partial derivatives in the preceding relations, the KS aggregation, low-order flutter analysis, structural model order reduction, and built-up FEM static solutions, are grouped as follows:

$$\underbrace{\frac{\partial \mathrm{KS}_{\mathrm{flutter}}}{\partial \boldsymbol{g}}}_{\text{KS aggregation}} \quad \underbrace{\frac{\partial \boldsymbol{g}}{\partial \hat{\boldsymbol{k}}}, \frac{\partial \boldsymbol{g}}{\partial \hat{\boldsymbol{m}}}, \frac{\partial \boldsymbol{g}}{\partial \hat{\boldsymbol{\delta}}}, \frac{\partial \boldsymbol{g}}{\partial \hat{\boldsymbol{\mathcal{I}}}}}_{\text{Low-order flutter analysis}} \quad \underbrace{\frac{\partial \hat{\boldsymbol{k}}}{\partial \hat{\boldsymbol{U}}}, \frac{\partial \hat{\boldsymbol{m}}}{\partial \boldsymbol{m}}, \frac{\partial \hat{\boldsymbol{\delta}}}{\partial \boldsymbol{m}}, \frac{\partial \hat{\boldsymbol{\mathcal{I}}}}{\partial \boldsymbol{m}}}_{\text{Model order reduction}} \quad \underbrace{\frac{\partial \boldsymbol{m}}{\partial \boldsymbol{M}_L}, \frac{\partial \hat{\boldsymbol{U}}}{\partial \hat{\boldsymbol{u}}_l}, \frac{\partial \hat{\boldsymbol{u}}_l}{\partial \boldsymbol{u}_l}}_{\text{Pre-processing}} \quad \underbrace{\frac{\partial \boldsymbol{u}_l}{\partial \boldsymbol{x}} = \boldsymbol{0}, \frac{\partial \mathbf{M_L}}{\partial \mathbf{x}}}_{\text{Built-up FEM}} \tag{42}$$

The calculation of these terms is discussed below.

2.2.3 Computing $\partial \boldsymbol{m}/\partial \boldsymbol{M}_L$ and $\partial \boldsymbol{M}_L/\partial \boldsymbol{x}$

The derivatives of the built-up FEM lumped mass matrix $\partial \boldsymbol{M}_L/\partial \boldsymbol{x}$ are provided by built-up FEM structural solver. See Kennedy and Martins [32] for details about the implementation used in this work. The operation $\boldsymbol{m} \rightarrow \boldsymbol{M}_L$ is a reduction operation, thus the derivative $\partial \boldsymbol{m}/\partial \boldsymbol{M}_L$ is a sparse matrix of zeros and ones.

2.2.4 Computing $\partial \hat{\boldsymbol{U}}/\partial \hat{\boldsymbol{u}}_l$ and $\partial \hat{\boldsymbol{u}}_l/\partial \boldsymbol{u}_l$

Extracting the displacement vectors $\hat{\boldsymbol{u}}_l$ associated with the beam reference axis nodes from the built-up FEM displacement vectors $\boldsymbol{u}_l$ is a mapping operation, while the assembly operations for stacking these elements into the vector $\boldsymbol{U}$ are permutation operations. The derivatives of these processes are sparse matrices of ones and zeros. For instance, $\partial \hat{\boldsymbol{U}}/\partial \hat{\boldsymbol{u}}_l$ is a permutation operation, resulting in a partially filled identity matrix that serves to select only the derivatives related to $\hat{\boldsymbol{u}}_l$.

2.2.5 Computing Equivalent Inertia Distribution Derivatives

The equivalent inertia distributions are differentiated analytically to compute the partial derivatives $\partial \hat{\boldsymbol{m}}/\partial \boldsymbol{m}$, $\partial \hat{\boldsymbol{\delta}}/\partial \boldsymbol{m}$, and $\partial \hat{\boldsymbol{\mathcal{I}}}/\partial \boldsymbol{m}$. For optimizations including only structural design variables, these derivatives are computed for fixed coordinates of the built-up FEM and beam reference axis nodes.

The mass $\hat{m}_j$ associated with the jth beam reference axis node ($j = 1, \ldots, \hat{N}$) is the sum of the nodal masses of the N_j built-up FEM nodes of its nearest neighbor:

$$\hat{m}_j = \sum_{i=1}^{N_j} m_i \tag{43}$$

The derivative of Eq. (43) with respect to the mass m_k associated with the kth built-up FEM node in the nearest neighbor of the jth beam reference axis node is

$$\frac{\partial \hat{m}_j}{\partial m_k} = \sum_{i=1}^{N_j} \frac{\partial m_i}{\partial m_k} = 1 \tag{44}$$

If the kth built-up FEM node does not belong to the nearest neighbor of the jth beam reference axis node, its nodal mass does not play a role in Eq. (43) and its derivative, Eq. (44), is zero. Because Eq. (43) does not depend on the other components of the built-up FEM mass matrix, the associated derivatives are also zero.

The offset components $\hat{\delta}_{j_x}$, $\hat{\delta}_{j_y}$, and $\hat{\delta}_{j_z}$ of the mass $\hat{m}_j$ associated with the jth beam reference axis node are

$$\hat{\delta}_{j_x} = \frac{1}{\hat{m}_j} \sum_{i=1}^{N_j} m_i \left(p_{i_x} + \delta_{i_x} - \hat{p}_{j_x}\right) \quad \hat{\delta}_{j_y} = \frac{1}{\hat{m}_j} \sum_{i=1}^{N_j} m_i \left(p_{i_y} + \delta_{i_y} - \hat{p}_{j_y}\right) \quad \hat{\delta}_{j_z} = \frac{1}{\hat{m}_j} \sum_{i=1}^{N_j} m_i \left(p_{i_z} + \delta_{i_z} - \hat{p}_{j_z}\right) \tag{45}$$

The derivatives of Eq. (45) with respect to the built-up FEM mass matrix data are reported for $\hat{\delta}_{j_x}$ only because the derivatives for the other mass offset components in Eq. (45) are given by similar relations.

The derivative of $\hat{\delta}_{j_x}$ with respect to the mass m_k associated with the kth built-up FEM node in the nearest neighbor of the jth beam reference axis node is given by

$$\frac{\partial \hat{\delta}_{j_x}}{\partial m_k} = \frac{1}{\hat{m}_j}[(p_{k_x} + \delta_{k_x}) - (\hat{p}_{j_x} + \hat{\delta}_{j_x})] \tag{46}$$

The derivatives with respect to the mass offset components associated with the kth built-up FEM node are

$$\frac{\partial \hat{\delta}_{j_x}}{\partial \delta_{k_x}} = \frac{m_k}{\hat{m}_j} \qquad \frac{\partial \hat{\delta}_{j_y}}{\partial \delta_{k_y}} = 0 \qquad \frac{\partial \hat{\delta}_{j_z}}{\partial \delta_{k_z}} = 0 \tag{47}$$

If the kth built-up FEM node does not belong to the nearest neighbor of the jth beam reference axis node, the derivatives (46) and (47) are zero. Because Eq. (43) does not depend on the built-up FEM inertia tensor data, the associated derivatives are also zero.

The independent components of the inertia tensor associated with the jth beam reference axis node ($j = 1, \ldots, \hat{N}_j$) about the local center of mass are given by

$$\begin{aligned}
\hat{\mathcal{I}}_{j_{xx}} &= \sum_{i=1}^{N_j} \mathcal{I}_{i_{xx}} + \sum_{i=1}^{N_j} m_i \left\{[(p_{i_y} + \delta_{i_y}) - (\hat{p}_{j_y} + \hat{\delta}_{i_y})]^2 + [(p_{i_z} + \delta_{i_z}) - (\hat{p}_{j_z} + \hat{\delta}_{j_z})]^2\right\} \\
\hat{\mathcal{I}}_{j_{yy}} &= \sum_{i=1}^{N_j} \mathcal{I}_{i_{yy}} + \sum_{i=1}^{N_j} m_i \left\{[(p_{i_x} + \delta_{i_x}) - (\hat{p}_{j_x} + \hat{\delta}_{j_x})]^2 + [(p_{i_z} + \delta_{i_z}) - (\hat{p}_{j_z} + \hat{\delta}_{j_z})]^2\right\} \\
\hat{\mathcal{I}}_{j_{zz}} &= \sum_{i=1}^{N_j} \mathcal{I}_{i_{zz}} + \sum_{i=1}^{N_j} m_i \left\{[(p_{i_x} + \delta_{i_x}) - (\hat{p}_{j_x} + \hat{\delta}_{j_x})]^2 + [(p_{i_y} + \delta_{i_y}) - (\hat{p}_{j_y} + \hat{\delta}_{j_y})]^2\right\} \\
\hat{\mathcal{I}}_{j_{xy}} &= \sum_{i=1}^{N_j} \mathcal{I}_{i_{xy}} - \sum_{i=1}^{N_j} m_i \left[(p_{i_x} + \delta_{i_x}) - (\hat{p}_{j_x} + \hat{\delta}_{j_x})\right]\left[(p_{i_y} + \delta_{i_y}) - (\hat{p}_{j_y} + \hat{\delta}_{j_y})\right] \\
\hat{\mathcal{I}}_{j_{xz}} &= \sum_{i=1}^{N_j} \mathcal{I}_{i_{xz}} - \sum_{i=1}^{N_j} m_i \left[(p_{i_x} + \delta_{i_x}) - (\hat{p}_{j_x} + \hat{\delta}_{j_x})\right]\left[(p_{i_z} + \delta_{i_z}) - (\hat{p}_{j_z} + \hat{\delta}_{j_z})\right] \\
\hat{\mathcal{I}}_{j_{yz}} &= \sum_{i=1}^{N_j} \mathcal{I}_{i_{yz}} - \sum_{i=1}^{N_j} m_i \left[(p_{i_y} + \delta_{i_y}) - (\hat{p}_{j_y} + \hat{\delta}_{j_y})\right]\left[(p_{i_z} + \delta_{i_z}) - (\hat{p}_{j_z} + \hat{\delta}_{j_z})\right]
\end{aligned} \tag{48}$$

The derivatives of Eq. (48) with respect to the built-up FEM lumped mass matrix data are reported for the $\hat{\mathcal{I}}_{j_{xx}}$ and $\hat{\mathcal{I}}_{j_{xy}}$ components because the derivatives for the other diagonal and off-diagonal components in Eq. (48) are given by similar relations.

The derivatives of $\hat{\mathcal{I}}_{j_{xx}}$ with respect to the mass m_k associated with the kth built-up FEM node in the nearest neighbor of the jth beam reference axis node is given by

$$\frac{\partial \hat{\mathcal{I}}_{j_{xx}}}{\partial m_k} = [(p_{k_y} + \delta_{k_y}) - (\hat{p}_{j_y} + \hat{\delta}_{j_y})]^2 + [(p_{k_z} + \delta_{k_z}) - (\hat{p}_{j_z} + \hat{\delta}_{j_z})]^2 \tag{49}$$

The derivatives with respect to the mass offset components associated with the kth built-up FEM node are

$$\frac{\partial \hat{\mathcal{I}}_{j_{xx}}}{\partial \delta_{k_x}} = 0 \qquad \frac{\partial \hat{\mathcal{I}}_{j_{xx}}}{\partial \delta_{k_y}} = 2\, m_k \left[(p_{k_y} + \delta_{k_y}) - (\hat{p}_{j_y} + \hat{\delta}_{j_y})\right] \qquad \frac{\partial \hat{\mathcal{I}}_{j_{xx}}}{\partial \delta_{k_z}} = 2\, m_k \left[(p_{k_z} + \delta_{k_z}) - (\hat{p}_{j_z} + \hat{\delta}_{j_z})\right] \tag{50}$$

The derivatives with respect to the inertia tensor components for the kth built-up FEM node are

$$\frac{\partial \hat{\mathcal{I}}_{j_{xx}}}{\partial \mathcal{I}_{k_{xx}}} = 1 \qquad \frac{\partial \hat{\mathcal{I}}_{j_{xx}}}{\partial \mathcal{I}_{k_{yy}}} = 0 \qquad \frac{\partial \hat{\mathcal{I}}_{j_{xx}}}{\partial \mathcal{I}_{k_{zz}}} = 0 \qquad \frac{\partial \hat{\mathcal{I}}_{j_{xx}}}{\partial \mathcal{I}_{k_{xy}}} = 0 \qquad \frac{\partial \hat{\mathcal{I}}_{j_{xx}}}{\partial \mathcal{I}_{k_{xz}}} = 0 \qquad \frac{\partial \hat{\mathcal{I}}_{j_{xx}}}{\partial \mathcal{I}_{k_{yz}}} = 0 \tag{51}$$

If the kth built-up FEM node does not belong to the nearest neighbor of the jth beam reference axis node, the derivatives (49) to (51) are all zero.

For the off-diagonal component $\hat{\mathcal{I}}_{j_{xy}}$, Eq. (49) becomes

$$\frac{\partial \hat{\mathcal{I}}_{j_{xy}}}{\partial m_k} = -[(p_{k_x} + \delta_{k_x}) - (\hat{p}_{j_x} + \hat{\delta}_{j_x})][(p_{k_y} + \delta_{k_y}) - (\hat{p}_{j_y} + \hat{\delta}_{j_y})] \tag{52}$$

Equation (50) becomes

$$\frac{\partial \hat{\mathcal{I}}_{j_{xy}}}{\partial \delta_{k_x}} = -m_k \left[(p_{k_y} + \delta_{k_y}) - (\hat{p}_{j_y} + \hat{\delta}_{j_y})\right] \qquad \frac{\partial \hat{\mathcal{I}}_{j_{xy}}}{\partial \delta_{k_y}} = -m_k \left[(p_{k_x} + \delta_{k_x}) - (\hat{p}_{j_x} + \hat{\delta}_{j_x})\right] \qquad \frac{\partial \hat{\mathcal{I}}_{j_{xy}}}{\partial \delta_{k_z}} = 0 \tag{53}$$

Finally:

$$\frac{\partial \hat{\mathcal{I}}_{j_{xy}}}{\partial \mathcal{I}_{k_{xx}}} = 0 \qquad \frac{\partial \hat{\mathcal{I}}_{j_{xy}}}{\partial \mathcal{I}_{k_{yy}}} = 0 \qquad \frac{\partial \hat{\mathcal{I}}_{j_{xy}}}{\partial \mathcal{I}_{k_{zz}}} = 0 \qquad \frac{\partial \hat{\mathcal{I}}_{j_{xy}}}{\partial \mathcal{I}_{k_{xy}}} = 1 \qquad \frac{\partial \hat{\mathcal{I}}_{j_{xy}}}{\partial \mathcal{I}_{k_{xz}}} = 0 \qquad \frac{\partial \hat{\mathcal{I}}_{j_{xy}}}{\partial \mathcal{I}_{k_{yz}}} = 0 \tag{54}$$

If the kth built-up FEM node is not in the nearest neighbor of the jth beam reference axis node, the derivatives (52) to (54) are zero.

The analytical derivatives in this section are simplified using the definition of local center of mass associated with the kth beam reference axis node:

$$\begin{aligned}
&\frac{1}{\hat{m}_j} \sum_{i=1}^{N_j} m_i[(p_{i_x} + \delta_{i_x}) - (\hat{p}_{j_x} + \hat{\delta}_{j_x})] = 0 \\
&\frac{1}{\hat{m}_j} \sum_{i=1}^{N_j} m_i[(p_{i_y} + \delta_{i_y}) - (\hat{p}_{j_y} + \hat{\delta}_{j_y})] = 0 \\
&\frac{1}{\hat{m}_j} \sum_{i=1}^{N_j} m_i[(p_{i_z} + \delta_{i_z}) - (\hat{p}_{j_z} + \hat{\delta}_{j_z})] = 0
\end{aligned} \tag{55}$$

The derivatives with respect to the built-up FEM offsets and inertia tensors are reported for completeness. However, they are not used in this work where these quantities are associated only with rigid-body elements representing non-structural mass distributions, which are not optimized.

2.2.6 Computing Equivalent Stiffness Distribution Derivatives

The equivalent stiffness distributions in Fig. (1) are differentiated numerically using the complex-step method to compute the partial derivatives $\partial \hat{\boldsymbol{k}}/\partial \hat{\boldsymbol{U}}$. A finite-difference implementation is developed for verification.

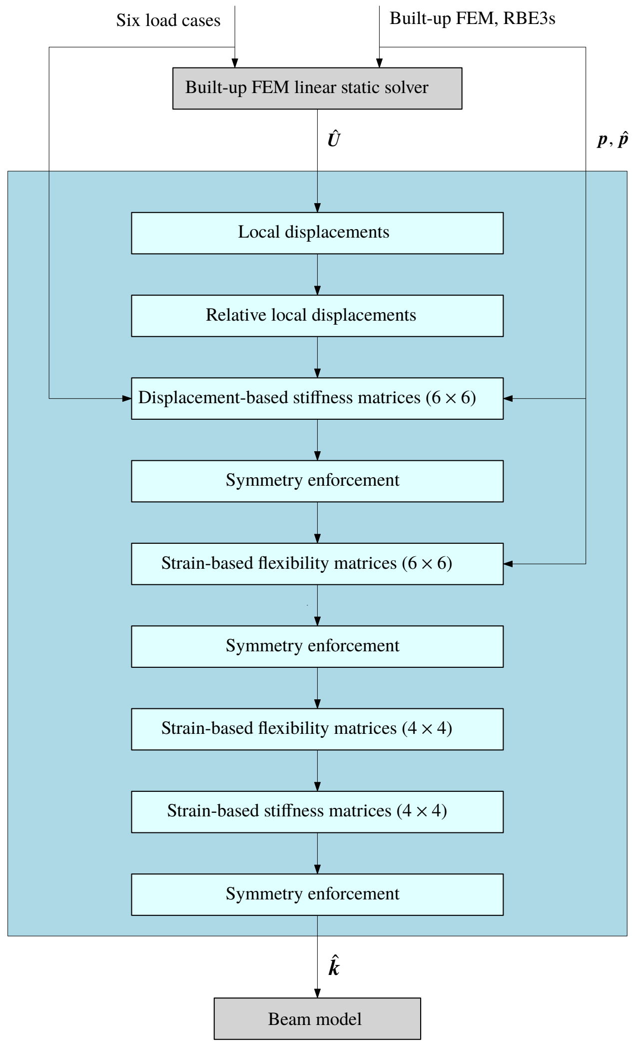

Figure 2: Computational procedure for equivalent stiffness module.

Figure 2 shows a schematic of the equivalent stiffness identification (see Refs. [25, 26] for details). The stiffness module inputs are the $3N \times 1$ vector $\mathbf{p}$ that lists the built-up FEM node coordinates, the $3\hat{N} \times 1$ vector $\hat{\mathbf{p}}$ that lists the coordinates of the beam reference axis nodes, and the $36\hat{N} \times 1$ vector $\hat{\mathbf{U}}$ of the built-up FEM static displacements (translations and rotations) for the six static load cases given at the beam reference axis nodes. The module output is the $10(\hat{N}-1) \times 1$ vector $\hat{\boldsymbol{k}}$ of the equivalent stiffness distributions that define the low-order beam representation of the built-up FEM, based on the formulation of Su and Cesnik [22]. The built-up FEM and beam reference axis node coordinates, listed in the vectors $\mathbf{p}$ and $\hat{\mathbf{p}}$, are constant in structural optimizations. Thus, the equivalent stiffness module provides only the partials $\partial\hat{\mathbf{k}}/\partial\hat{\mathbf{U}}$.

2.2.7 Computing Flutter Analysis and Aggregation Derivatives

The flutter analysis and constraint aggregation are differentiated in part analytically and in part using automated differentiation (AD) to compute the partial derivatives $\partial\boldsymbol{g}/\partial\hat{\boldsymbol{k}}$, $\partial\boldsymbol{g}/\partial\hat{\boldsymbol{m}}$, $\boldsymbol{\partial g/\partial\hat{\delta}}$ and $\boldsymbol{\partial g/\partial\hat{\mathcal{I}}}$ and $\partial\mathrm{KS}_{\mathrm{flutter}}/\partial\boldsymbol{g}$.

The flutter analysis involves linearizing the equations of motion about the nonlinear equilibrium states at selected flight conditions to obtain linearized equations in the time-domain state-space form of Eq. (16). An eigenvalue analysis is conducted on the full state-space matrix directly (no modal reduction) using standard eigenvalue analysis techniques (no p–k or other equivalent frequency-domain flutter analysis methods). Because the state-space matrix is computed by linearizing the equations of motion about each nonlinear equilibrium state, its eigenvalues and eigenvectors reflect the dynamic characteristics of the statically deformed shape at that flight condition. Once the eigenvalues of each linearized system are available, their real parts (damping values) are constrained to lie below a bounding curve. This allows the user to enforce a damping threshold different than zero at the various flight conditions for a more conservative flutter constraint, or to prevent its violation by marginally stable modes, or both. The bounded damping values are then KS-aggregated to obtain the scalar flutter constraint in Eq. (20). This is done by first aggregating all the bounded damping values at each flight condition, and then by aggregating the resulting quantities over the flight conditions.

The linearization and eigenvalue analysis process leverages a nonlinear aeroelastic framework described in Sec. 3, the University of Michigan's Nonlinear Aeroelastic Simulation Toolbox (UM/NAST) [6] (see also Sec. 3.3). An AD-based module associated with UM/NAST was developed in this work to differentiate the nested KS aggregation for each flight condition, providing the partial derivatives of the aggregate values with respect to the equivalent beam inertia and stiffness distributions. The derivatives of the outer KS aggregation are the analytical derivatives of the KS function. Next, the two sets of derivatives are combined using the chain rule to compute the derivatives of the flutter constraint with respect to the equivalent beam distributions. A finite-difference calculation is developed for verifying the AD implementation.

3 Computational Implementation

This section describes the computational framework that implements the methodology of Sec. 2. While the various modules already existed, they have been coupled in this work for the first time to bring the geometrically nonlinear flutter constraint in high-fidelity gradient-based wing structural optimizations. Additionally, some modules have been differentiated to obtain missing partial derivatives. Finally, the partial derivatives of all modules have been integrated in the new adjoint formulation to obtain the total derivatives of the geometrically nonlinear flutter constraint with respect to the detailed structural sizing variables.

3.1 Optimization Algorithm

The optimization algorithm is SNOPT (Sparse Nonlinear OPTimizer) [33], a gradient-based optimizer that implements a sequential quadratic programming (SQP) algorithm. SNOPT uses an augmented Lagrangian merit function; the Hessian of the Lagrangian is approximated using a quasi-Newton approach that is suited to optimization problems with many sparse nonlinear constraints. The interface with SNOPT is handled by pyOptSparse[1] [34], an implementation of pyOpt [35] that eases the process of defining large sparse Jacobians crucial to the performance of large scale optimizers like SNOPT.

3.2 High-Fidelity Structural Analysis

The structural analysis solver is the Toolkit for the Analysis of Composite Structures (TACS) [32].[2], an open-source parallel finite element solver that handles poorly conditioned problems common in aircraft thin-walled structures. For such cases, the stiffness matrix condition numbers may exceed

[1] https://github.com/mdolab/pyoptsparse
[2] https://github.com/smdogroup/tacs

$\mathcal{O}(10^9)$, but TACS can solve these poorly conditioned problems using a Schur-complement-based parallel direct solver. Sensitivities of structural functions of interest with respect to structural and geometric design variables are computed efficiently using the adjoint method [32, 36]. In this work, TACS computes the mass matrix and static displacements used for the mass and stiffness condensation process and computes the structural mass objective function and stress constraints during optimization.

3.3 Low-Order Flutter Analysis

The geometrically nonlinear flutter constraint is based on damping values from aeroelastic eigenvalue analyses about the equilibrium states at selected flight conditions. The eigenvalue analyses are conducted in UM/NAST [6], a low-order multidisciplinary framework for modeling, analyzing, and simulating very flexible wings and complete aircraft in free flight.

UM/NAST describes an aircraft as a set of beams representing different components (wing, fuselage, etc.) that undergo arbitrarily large structural deflections relative to a body-fixed frame in motion with respect to an inertial frame. Structural deflections are described by the geometrically exact strain-based beam formulation of Su and Cesnik [22], which uses element strains (extension, twist, and bending curvatures) as the independent DOFs and recovers the deformed shape by integrating nonlinear kinematic relations [6, 22].

UM/NAST handles different loads including gravity, point/distributed forces and moments, and aerodynamics. Aerodynamic loads can be computed using multiple formulations. In this work, we use the potential flow unsteady airfoil theory of Peters *et al.* [27], a time-domain unsteady aerodynamic model suitable to obtain aeroelastic equations in state-space form. This formulation assumes strip theory: the aerodynamic loads at the cross-sections of the beam element nodes depend only on the local flow and control parameters (angle of attack, Mach number, control-surface deflections). These aerodynamic loads can be corrected for compressibility, sweep, or tip losses. Unsteady aerodynamic effects are captured by a set of aerodynamic states representing inflow expansions [27].

This work leverages the UM/NAST ability to compute aeroelastic eigenvalues of geometrically nonlinear wings (and complete aircraft) by accounting for their in-flight deflections. The process [6] starts with numerically linearizing the equations of motion about the nonlinear equilibrium states of the system at chosen flight conditions. This gives a time-domain linearized state-space model in the form of Eq. (16) for each flight condition, with state variables given by the strain measures, their rates, and the unsteady aerodynamic states of the theory of Peters *et al.* [27]. The linearization process for each flight condition captures the changes in the steady and unsteady aerodynamic characteristics with the equilibrium state (that is, the wing or aircraft static aeroelastic deflection).

The eigenvalues of the full-order state-space matrix associated with each linearized system are obtained using a standard eigenvalue analysis (not the p–k method), as the theory of Peters *et al.* [27] provides unsteady aerodynamic loads in the time domain. The eigenvectors associated with the obtained eigenvalues are the aeroelastic mode shapes of the statically deformed configurations at a given flight condition, about which the equations of motion are linearized.

Once the eigenvalues are known for all the flight conditions of interest, they are used for evaluating the flutter constraint or further post-processed for computing the flutter boundary for analysis purposes. The flutter constraint and derivative evaluation discussed in Sec. 2.2.7 is handled by an in-house developed wrapper based on OpenMDAO routines[3] [37] that couples the UM/NAST component with the rest of the framework. OpenMDAO facilitates the coupling of the models and the coupled derivative computation.

[3] `https://github.com/OpenMDAO/OpenMDAO`

Note that the nonlinear equilibrium states of the system at the flight conditions considered for the flutter constraint are computed in UM/NAST directly on the beam representation associated with the built-up FEM at each optimization step. This increases the computational efficiency and robustness of the flutter constraint because detailed nonlinear static aeroelastic analyses based on the built-up FEM are impractical for optimization due to the high computational cost and potential convergence issues. The impact of computing the nonlinear equilibrium states on the beam model, instead of mapping it from the built-up FEM, is not investigated in this work. However, recent extensive studies compared the impact of model complexity on aeroelastic solution accuracy for very flexible wings [19, 28]. These studies found that a parent built-up FEM and its derived beam representation predict the same nonlinear structural and aeroelastic deformed shapes up to very large wingtip deflections of the order of 40% semispan. Further, geometrically nonlinear flutter analyses based on the beam model captured experimental flutter points for a range of wing deflections with errors below 4%. These results corroborate the choice of using models of different complexity but with similar accuracy within the same optimization process to predict the stress and flutter constraints.

3.4 Structural Model Order Reduction

To evaluate the geometrically nonlinear flutter constraint, it requires reducing the TACS built-up FEM at a given optimization step to a low-order beam representation in UM/NAST (see Sec. 2). The equivalent beam distributions of the TACS built-up FEM are computed using the University of Michigan's Enhanced FEM2Stick (UM/EF2S) code [25, 26], which has been enhanced with derivative capabilities for this work. The outputs from EF2S are fed to UM/NAST to compute the geometrically nonlinear flutter constraint and its derivatives with respect to the equivalent inertia and stiffness distributions. The total derivatives of the geometrically nonlinear flutter constraint with respect to the built-up FEM structural design variables are obtained from the adjoint formulation in Sec. 2.2.

4 Optimization Problem

This section describes the optimization problem used for demonstrating the methodology. Section 4.1 describes the baseline model and Sec. 4.2 reports the optimization problem statement.

4.1 Baseline Model

The baseline model is shown in Fig. 3. The model consists of a rectangular, untwisted wing with a unit chord, an aspect ratio of 12, and a constant NACA 0012 aerodynamic cross section. The structure is made of an isotropic 2024-T3 aluminum material with density of 2780 kg/m^3, Young's modulus of 73.1 GPa, and tensile yield strength of 345 MPa. The wingbox spans from 15% to 65% of the aerodynamic chord, and its sizing is determined from a preliminary structural optimization under representative 2.5-g aerodynamic loads without a flutter constraint. The resulting optimized structural mass is 68.5 kg. This pre-optimized wingbox model provided the baseline design for the subsequent flutter-constrained optimization. The model is completed by three 15 kg non-structural point masses along the trailing edge at each third of the semispan, which are included in the beam model as rigid-body elements that are not optimized. These masses are added to make the baseline model flutter over a range of flight speeds and wing-root angles of attack, resulting in a sensible range of static deflections. The masses also help keep the flutter onset speed within a speed range where the potential flow theory holds.

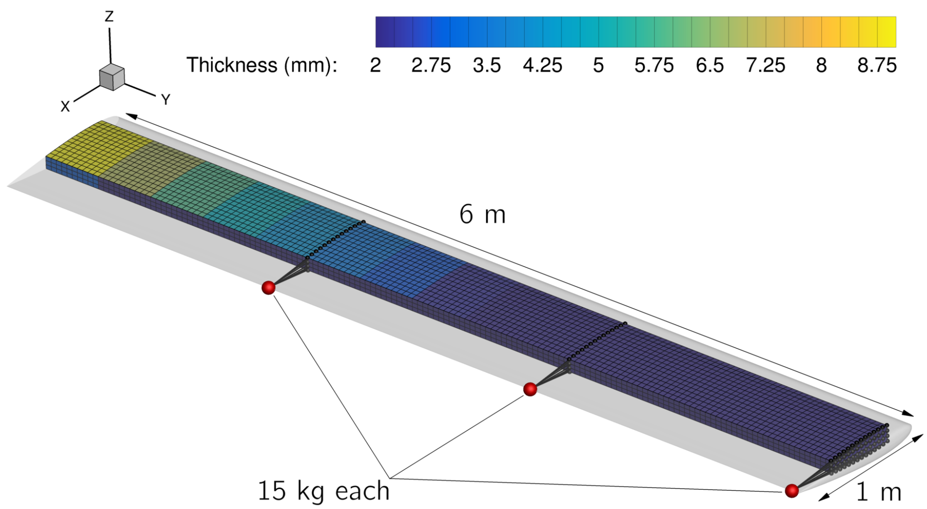

Figure 3: Baseline wing model.

The built-up FEM wingbox in TACS is condensed to an equivalent beam model in UM/NAST to evaluate the geometrically nonlinear flutter constraint at each optimization step. The beam reference axis is at 41% of the aerodynamic chord and is discretized in 7 elements along the span. This corresponds to 8 spanwise beam nodes at the beam element ends. While UM/NAST uses a three-node beam element, only the element end nodes are used in the stiffness identification because the geometrically exact strain-based beam formulation implemented into the framework assumes element-uniform stiffness properties. Each beam reference axis node is connected to its cross section's leading and trailing edge nodes by an interpolation element akin to an MSC Nastran RBE3. Figure 4 shows the TACS and UM/NAST models overlapped. The UM/NAST beam model is coupled to a potential flow unsteady thin airfoil model [27] with a zero-thickness, flat-plate cross-section. Subsonic compressibility effects are captured by the Prandtl–Glauert correction. Unsteady aerodynamic effects are modeled by adding six inflow states per element [27]. Three-dimensional aerodynamic effects are not considered in the flutter analysis. However, they can be added, for instance, using tip loss factors or by specifying a variable lift curve slope along the span based on a detailed aerodynamic model. Transonic effects could be incorporated by replacing the theory of the current potential flow approach with an aerodynamic model appropriate for transonic regimes (*e.g.*, [11, 38]). This is however beyond the scope of the present work.

The low-order aeroelastic model is used for evaluating the geometrically nonlinear flutter constraint, while the other functions of interest are evaluated on the built-up FEM. This is capable of capturing detailed structural features and their influence on the wing mass and peak stress levels, while keeping geometrically nonlinear flutter analyses computationally tractable for optimization. Integrating models of different complexity in the same gradient-based optimization is a major new contribution from this work, compared with previous flutter-constrained optimizations that included geometrically nonlinear effects [15–17].

4.2 Optimization Statement

Table 1 summarizes the optimization problem that demonstrates the methodology. The optimization minimizes the wingbox structural mass by varying the thickness of the skin, spar, and

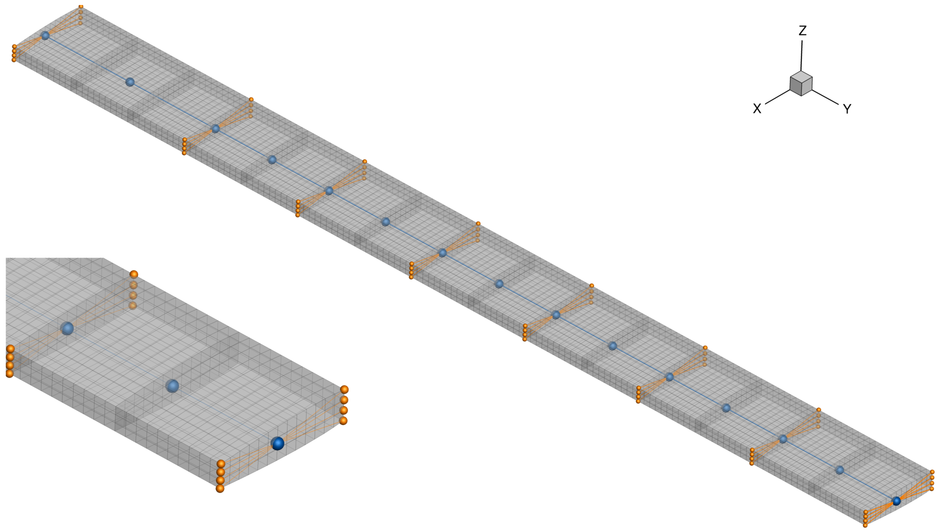

Figure 4: Baseline wing TACS and UM/NAST structural models.

rib panels. Each panel is treated as a non-stiffened shell element and given its thickness variable, resulting in 76 structural sizing variables. The non-structural point masses are kept constant during the optimization. Hence, they are not considered in the objective function, as doing so only adds a constant offset to the optimization results. The term "wingbox mass" hereafter refers to the structural mass only, and any numerical mass values reported do not include the non-structural point masses.

The primary constraint is the geometrically nonlinear flutter constraint evaluated in UM/NAST based on the formulation of Section 2.1. This constraint aggregates the damping values from a set of eigenvalue analyses at fixed root angle of attack and varying speed. The aggregation provides a continuous, smooth, and differentiable approximation to a given design's most positive damping value. The damping values are bounded by a threshold of 0.12 rad/s that is constant with speed and aggregated using an aggregation parameter $\rho_{\mathrm{KS}} = 100$ for all damping values. The threshold is introduced to avoid constraint violations associated with marginally stable in-plane modes, achieving a similar effect as adding structural damping. The aggregated flutter constraint value needs to be less than or equal to zero for the design to be feasible, with a value of zero indicating an active constraint.

The optimization also enforces stress constraints, which are evaluated directly on the built-up FEM. The stress constraint value on each element is computed using the von Mises stress failure criterion. For this constraint, a value less than or equal to one indicates a feasible design [32], differently from the flutter constraint that must be less or equal to zero for the design to be feasible. The stress constraints for groups of elements are then KS-aggregated to reduce the number of constraints to four: one for the upper skins, one for the lower skins, one for both spars, and one for the ribs. The element stresses are evaluated from linear static analyses of the built-up FEM under pre-computed loads representative of a 2.5-g maneuver, a typical aircraft sizing case, with a safety factor of 1.5. The pre-computed loads are obtained from an aerostructural analysis at sea level and Mach number of 0.5, using the built-up FEM in TACS coupled with ADflow, a parallel, finite-volume, cell-centered, multi-block aerodynamic solver [39].[4] The corresponding root angle of attack for this condition was solved for by enforcing the total lift to match the desired load factor of 2.5-g.

[4] https://github.com/mdolab/adflow

Table 1: Optimization formulation.

	Function/variable	Description	Unit	Quantity
minimize	M	Wingbox mass	kg	
with respect to	t	Panel thicknesses of skins/spars/ribs	m	76
subject to	$\mathrm{KS}_{\mathrm{flutter}} \leq 0$	KS aggregate of modal damping values	rad/s	1
	$\mathrm{KS}_{\mathrm{stress}} \leq 1$	KS aggregates of 2.5-g Yield stress values	Pa	4
	$\lvert t_{\mathrm{skin},\, i} - t_{\mathrm{skin},\, i+1} \rvert \leq 0.005$	Skin adjacency constraints	m	28
	$\lvert t_{\mathrm{spar},\, i} - t_{\mathrm{spar},\, i+1} \rvert \leq 0.005$	Spar adjacency constraints	m	28

Finally, the optimization includes a set of linear adjacency constraints that limit the thickness change between any two adjacent skin or spar panels to be less than 5 mm. These constraints enforce more realistic designs and improve the optimizer performance by limiting the design space, even in cases where the adjacency constraints are not active.

While buckling constraints are essential in practical wing sizing and may be critical design constraints, they are omitted here to limit the problem complexity for the purpose of demonstrating the geometrically nonlinear flutter constraint, which is the focus of this work. A complete optimization statement could include buckling constraints using either an eigenvalue analysis or a smeared stiffener approach [40, 41].

Three optimizations are solved by evaluating the geometrically nonlinear flutter constraint at different root angles of attack $\alpha = 0°, 3°$, and $6°$. These cases are considered to investigate how geometrically nonlinear effects associated with different wing in-flight deflection levels impact the optimized design. At zero root angle of attack, the geometrically nonlinear flutter constraint reduces to a linear flutter constraint for the undeformed shape. At a nonzero root angle of attack, the wing experiences static deflections that modify the flutter constraint value and lead to different optimized results. The flutter analysis considers sea-level altitude and the speed range $V = 10 \rightarrow 180$ m/s, sampled with 10 equally spaced points. These flight conditions are chosen to make the wing experience no, medium, and large static aeroelastic deflections at the three root angles of attack, respectively. In all optimizations, the stress constraints are computed on the linear built-up FEM (not on the beam model) based on the pre-computed loads for the 2.5-g maneuver, as described above. These loads are obtained offline and do not vary with the root angle of attack considered in the flutter analysis. This ensures that any changes in the optimized designs with the root angle of attack are due to the impact of wing in-flight deflections on the flutter characteristics. Additionally, the pre-computed loads are also the same as used in the preliminary structural optimization to size the baseline design for the flutter-constrained optimizations.

4.3 Derivative verification

The total derivatives of the geometrically nonlinear flutter constraint with respect to the built-up FEM structural sizing variables are verified by comparing the values computed from the developed adjoint formulation (Sec. 2.2) with a second-order central finite-difference approximation applied to the entire derivative chain:

$$\frac{d\boldsymbol{\mathcal{F}}}{d\boldsymbol{x}} = \frac{\boldsymbol{\mathcal{F}}(\boldsymbol{x}+h) - \boldsymbol{\mathcal{F}}(\boldsymbol{x}-h)}{2h} + O(h^2).$$

A step-size study is performed, and the resulting relative step used for the verification is $h = 10^{-3}$. Table 2 compares the derivatives for selected design variables computed using the finite-difference

Table 2: Verification of the total derivatives of the flutter constraint $KS_{flutter}$ with respect to selected structural design variables (relative finite-difference step size $h = 10^{-3}$).

Design variable	Derivative formulation: Finite difference	Adjoint	Δ (%)
$x_{\text{Rib 4}}$	−**14.1**08794	−**14.1**14520	4.0586×10^{-2}
$x_{\text{Front spar 4}}$	−**739.8**24090	−**739.8**09480	1.9747×10^{-3}
$x_{\text{Rear spar 4}}$	−**615.5**54519	−**615.5**48978	9.0021×10^{-4}
$x_{\text{Upper skin 12}}$	−**900.7**66347	−**900.7**53299	1.4486×10^{-3}
$x_{\text{Lower skin 12}}$	−**900**.415733	−**900**.398323	1.9335×10^{-3}

approximation and the adjoint formulation. The derivative values agree with each other for all design variables, showing relative errors from about 0.001% to 0.04%. The level of agreement for the total derivatives reported in Table 2 is representative of all the total derivatives. The average relative difference between the finite-difference and adjoint results is 0.005%.

5 Optimization Results

Table 3 summarizes the objective and constraint functions for all the optimized designs. The results for the objective function (structural mass) show both the absolute value and the penalty compared with the baseline design obtained from the pre-optimization without the flutter constraint. The results for the constraint functions show active constraints in black and inactive constraints as faded. The wingbox mass increases due to the flutter constraint, which is active (equal to zero) for all cases. When the flutter constraint is evaluated at $\alpha = 0°$, which corresponds to a linear flutter analysis of the undeformed shape, the resulting penalty is 11.1% of the baseline mass. When the flutter constraint is evaluated at $\alpha = 3°$ and $6°$, the wing experiences static aeroelastic deflections, which vary with the flow speed, resulting in a geometrically nonlinear flutter analysis. In these cases, the flutter constraint adds penalties of 38.1% and 52.7% of the baseline mass, respectively, more than three and five times the penalty for $\alpha = 0°$.

Table 3: Optimized wingbox structural mass and state of the constraints for each case (faded = inactive constraint).

		Flutter constraint root angle of attack		
	Baseline	Linear	Geometrically nonlinear	
	(no flutter constraint)	$\alpha = 0°$	$\alpha = 3°$	$\alpha = 6°$
Mass [kg]	68.5	76.1 (+11.1%)	94.6 (+38.1%)	104.6 (+52.7%)
$KS_{flutter}$	-	0.0	0.0	0.0
KS_{stress} for ribs	0.25	0.24	0.20	0.18
KS_{stress} for spars	0.75	0.69	0.65	0.67
KS_{stress} for upper skins	1.0	1.0	1.0	1.0
KS_{stress} for lower skins	1.0	1.0	0.98	0.89

The stress constraints on the ribs and spars are inactive (less than one), while the ones on the upper skins are always active (equal to one). The lower skin's stress constraints are active for the baseline design and when the flutter constraint is evaluated at $\alpha = 0°$ (linear case) but are inactive when the flutter constraint is evaluated at $\alpha = 3°$ and $\alpha = 6°$ (geometrically nonlinear cases). This can be explained by analyzing the optimized structural sizing and the von Mises stress failure criterion value, shown in Figs. 5 and 6, respectively, along with their differences compared with the baseline design. In the optimized designs, the thicknesses of the spars, upper, and lower skins increase with the root angle of attack considered in the flutter analysis. At nonzero root angle of attack, the increased thickness of the spars decreases the wing deflections, allowing the optimizer to satisfy the flutter constraint while lowering the skin stresses. The thickness also increases for the lower skins, more than for the upper skins, when the flutter constraint is evaluated at $\alpha = 3°$ and $\alpha = 6°$, compared with the baseline design and the optimized design for the linear case. This lowers the stress on the lower skins, resulting in an inactive constraint for the larger angles of attack. Because the stress analyses in all optimizations use the same pre-computed loads, these differences among the optimized designs can be directly attributed to the flutter constraint and its variation with the root angle of attack and the resulting range of wing deflections.

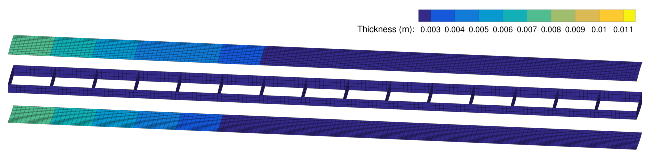

(a) Baseline sizing, optimized without flutter constraint

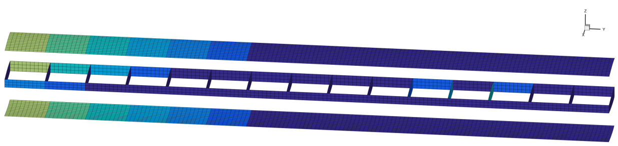

(b) Optimized sizing with flutter constraint for $\alpha = 0°$

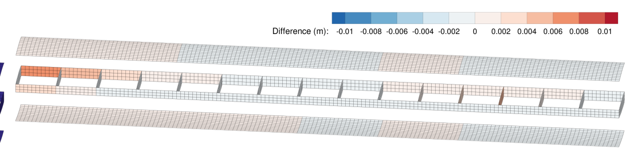

(c) Sizing difference with and without flutter constraint for $\alpha = 0°$

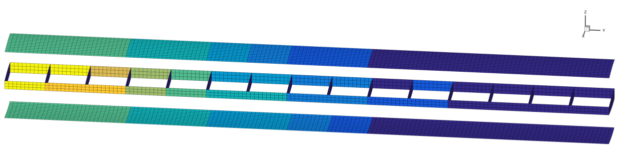

(d) Optimized sizing with flutter constraint for $\alpha = 3°$

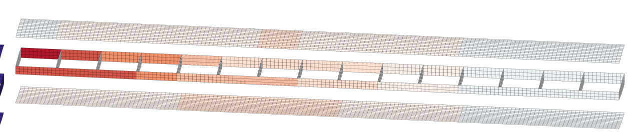

(e) Sizing difference with and without flutter constraint for $\alpha = 3°$

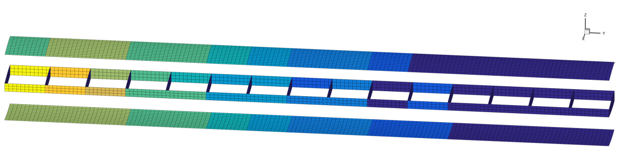

(f) Optimized sizing with flutter constraint for $\alpha = 6°$

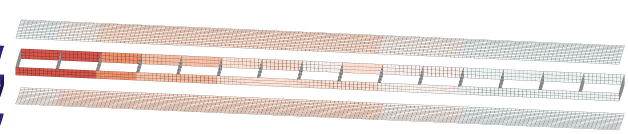

(g) Sizing difference with and without flutter constraint for $\alpha = 6°$

Figure 5: Comparison of the baseline and optimized structural sizing.

Table 4 shows a mass breakdown for each group of components. Relative mass variations for each optimized design are with respect to the mass value for the baseline model, which is pre-optimized without the flutter constraint. Except for the optimized design at $\alpha = 0°$, all ribs remain

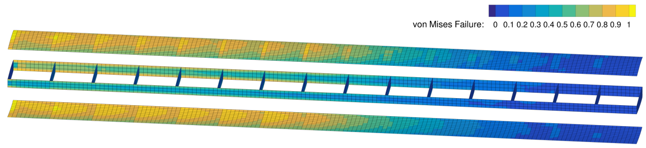

(a) Baseline failure values, optimized without flutter constraint

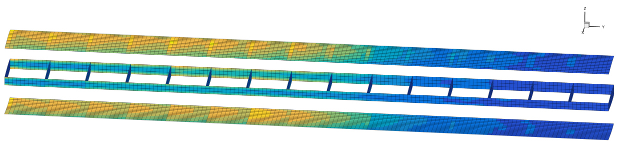

(b) Optimized failure values with flutter constraint for $\alpha = 0^{\circ}$

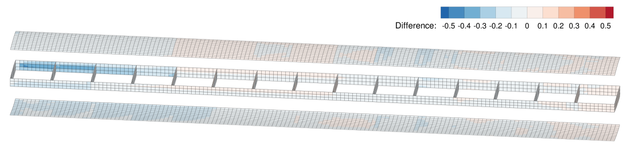

(c) Failure values difference with and without flutter constraint for $\alpha = 0^{\circ}$

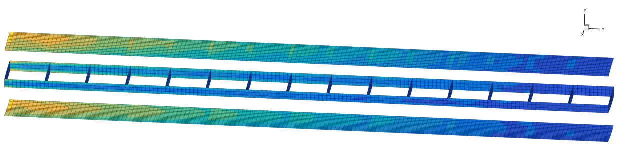

(d) Optimized failure values with flutter constraint for $\alpha = 3^{\circ}$

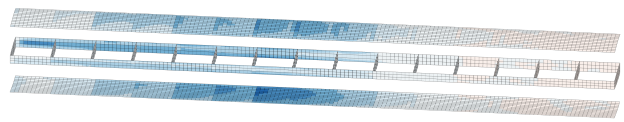

(e) Failure values difference with and without flutter constraint for $\alpha = 3^{\circ}$

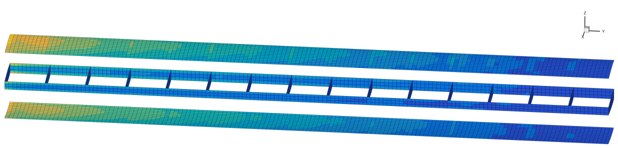

(f) Optimized failure values with flutter constraint for $\alpha = 6^{\circ}$

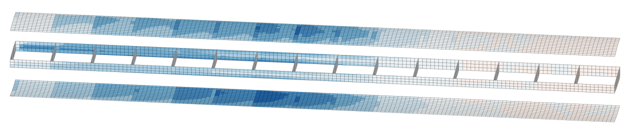

(g) Failure values difference with and without flutter constraint for $\alpha = 6^{\circ}$

Figure 6: Comparison of the baseline and optimized von Mises stress failure criterion values.

unchanged, at the lower bound, compared with the baseline wing. All optimized designs have thicker spars than the baseline, especially at the front. Increasing the spar thickness is the most mass efficient way for the optimizer to increase the wingbox torsional stiffness, mitigating flutter. Additionally, reinforcing the front and rear spars differently changes the bend-twist coupling of the wing as well as the elastic axis location, which also affect its flutter behavior. Reinforcing the front spar also has the effect of shifting the center of mass forward, which has stabilizing aeroelastic benefits. However, this is likely to be a negligible effect in this case, since the total mass of both wing spars is less than half the mass of the non-structural trailing edge masses.

The mass of the upper and lower skins increases compared with the baseline design, particularly in the $\alpha = 3^{\circ}$ and $\alpha = 6^{\circ}$ cases. This can be attributed to a different flutter mechanism for those root angles of attack cases compared with the $\alpha = 0^{\circ}$ case, as shown in Table 5. At zero root angle of attack, the flutter mechanism involves the coupling of out-of-plane bending and torsion, which the optimizer delays by mainly thickening the front spar.

At a nonzero root angle of attack, the wing's vertical deflection leads to a geometrically nonlinear coupling between in-plane bending and torsion [4], causing the originally in-plane bending mode (mode 2) to transform into a 3-DOF flutter mechanism. In this case, the optimizer further increases the spar and skin thicknesses compared to the flutter constraint evaluated at $\alpha = 0^{\circ}$. Increasing the thickness of the spars stiffens the wing in in-plane bending and torsion while increasing the skin

Table 4: Breakdown of the optimized wingbox structural mass and change relative to the baseline design.

	Baseline (no flutter constraint)	Flutter constraint root angle of attack					
		Linear		Geometrically nonlinear			
		$\alpha = 0°$		$\alpha = 3°$		$\alpha = 6°$	
Group	Mass [kg]	Mass [kg]	Δ[%]	Mass [kg]	Δ[%]	Mass [kg]	Δ[%]
Ribs	4.8	6.3	30.2	4.8	0.0	4.8	0.0
Front spar	3.4	5.5	61.4	9.4	173.3	9.0	161.8
Rear spar	2.8	3.1	11.9	7.7	176.0	7.3	161.5
Upper skin	29.4	29.8	1.2	35.9	21.9	40.9	39.1
Lower skin	28.1	30.4	8.5	36.9	31.5	42.6	52.0

Table 5: Baseline critical flutter speed and the associated aeroelastic mode for each case.

$\alpha[\circ]$	V_f [m/s]	Flutter mode #
0	151.7	4
3	145.1	2
6	137.9	2

thicknesses reduces the wing deflections, in turn reducing the coupling of in-plane bending with torsion and helping mitigate flutter.

The optimizer trades off increasing the thicknesses of skins and spars to satisfy the flutter constraint while minimizing the mass penalty. When the flutter constraint is evaluated at root angle of attack of $\alpha = 3°$, the optimizer finds it more effective to thicken the spar. To satisfy the flutter constraint at $\alpha = 6°$, the optimizer chooses to increase the skin thickness even further, but the spars show a smaller increase than for $\alpha = 3°$. This result suggests that reducing in-flight deflections to restrict the in-plane bending-torsion coupling is a more mass-effective flutter suppression strategy at larger root angles of attack compared with increasing in-plane bending and torsional stiffness.

The optimized structural sizing is reflected in the static aeroelastic response. Figure 7 shows the wing displacements normalized by the semispan and the twist angle spanwise distribution for all cases at the maximum speed of 180 m/s considered in the flutter analyses. The out-of-plane bending tip displacements of the baseline design range from 0–50% of the semispan, which reduces to 0–29% semispan for the optimized designs, with attenuated shortening effects. Twist angles are also smaller for the optimized designs, demonstrating close to a linear twist distribution, while for the baseline design, it flattens around the tip due to geometrically nonlinear effects. The smaller static aeroelastic deflections of the optimized designs result from the increased skin thickness, which stiffens the structure.

Figure 8 and Table 6 show the structural mode shapes and frequencies for the undeformed baseline and optimized designs, where OOP, IP, and T refer to out-of-plane bending, in-plane bending, and torsion modes respectively. The mode shapes are computed on the beam model to better focus on the global OOP, IP, and T behaviors, which can be readily identified from the bending displacements and twist rotations of the reference axis. The concentrated masses at the

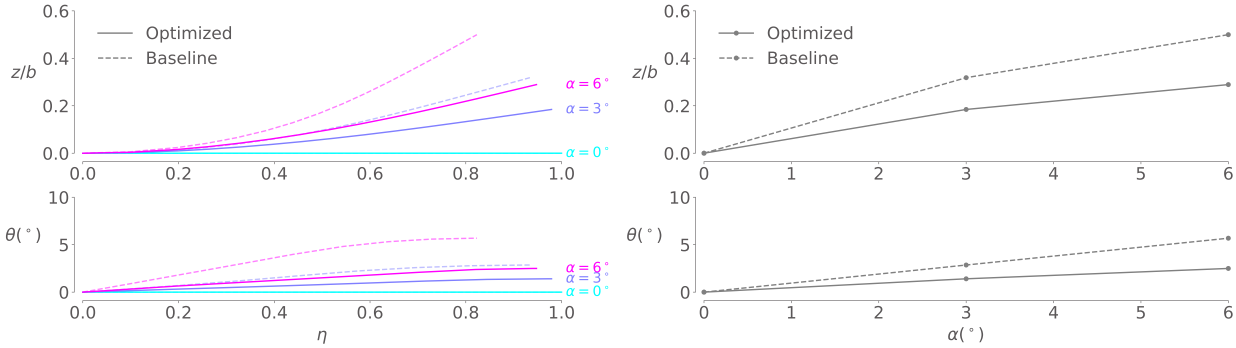

(a) Static aeroelastic displacement and twist angle along the span

(b) Static aeroelastic tip displacement and twist angle

Figure 7: Static aeroelastic response of the baseline and optimized designs at $V = 180\,\mathrm{m/s}$.

trailing edge couple OOP bending and torsion modes, causing no pure torsional modes but coupled bending-torsion modes. While the mode shapes are similar across all designs, the frequency values and separation increase with the root angle of attack considered in the flutter constraint because of the added structural thickness. Note that the structural mode shapes and frequencies are reported for completeness and to explore the impact of the flutter constraint root angle of attack on the wing vibration features. They are not used in the aeroelastic eigenvalue analyses for evaluating the flutter constraint. The eigenvalue analyses are conducted on the full-order state-space matrix of the aeroelastic system linearized about each flight condition, not on a set of modal equations defined using structural mode shapes (which is the common practice in linear flutter analysis solvers), as discussed in Secs. 2 and 3.

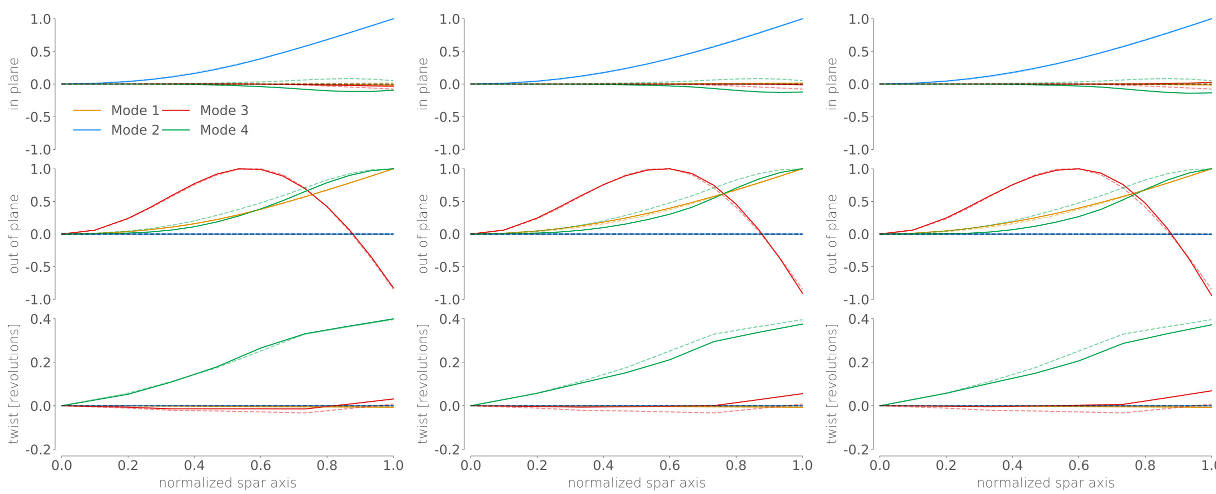

(a) $\alpha = 0°$

(b) $\alpha = 3°$

(c) $\alpha = 6°$

Figure 8: Mode shapes of the undeformed baseline (dash) and optimized (solid) designs.

The flutter constraint is active for all optimized designs, as highlighted in the damping plots of Fig. 9. While the flutter analysis considers all aeroelastic DOFs, only the first four modes are visualized to highlight the flutter point. Figure 10 compares the optimized and baseline designs.

Table 5 contains the flutter speed and associated aeroelastic modes of the baseline design for

Table 6: In-vacuum structural frequencies of the undeformed baseline and optimized wingbox configurations.

		Baseline (no flutter constraint)	Flutter constraint root angle of attack					
			Linear		Geometrically nonlinear			
			$\alpha = 0°$		$\alpha = 3°$		$\alpha = 6°$	
Mode	Type	f [Hz]	f [Hz]	Δ[%]	f [Hz]	Δ[%]	f [Hz]	Δ[%]
1	OOP1	3.44	3.47	0.9	4.01	16.6	4.26	23.8
2	IP1	10.24	10.60	3.5	13.47	31.5	13.86	35.4
3	OOP2	17.07	17.65	3.4	17.63	3.3	18.13	6.2
4	OOP1+T1	28.37	28.69	1.1	34.32	21.0	36.11	27.3

each of the three root angle-of-attack cases. The critical aeroelastic mode is labeled according to their frequency order. The baseline design is flutter critical for each root angle of attack. In contrast, the unstable modes are pushed below the 0.12 rad/s damping threshold for all optimized designs at the speed points used in the optimization.

The flutter mechanism varies with the root angle of attack due to the different wing static deflections. When the flutter constraint is evaluated at $\alpha = 0°$, the wing remains undeformed at all speeds. The two fluttering modes for the baseline design are modes 3 and 4, which involve coupled out-of-plane bending and torsion. By increasing the front spar thickness, the optimizer increases the frequencies of these modes and reduces their coupling to delay flutter. Mode 2, an in-plane bending mode, is unaffected by the optimization because it does not interact with aerodynamics for this case. When the flutter constraint is evaluated at a nonzero root angle of attack, the wing experiences static deflections, which vary with speed. In these cases, the previously described 3 DOF mode that originates from the in-plane structural mode 2 is the critical flutter mode for the baseline design and the $\alpha = 3°$ and $\alpha = 6°$ optimized designs. As already mentioned, this behavior is driven by the geometrically nonlinear coupling of in-plane bending and torsion in the presence of wing deflections, which the optimizer mitigates by increasing the wingbox skin and spar thicknesses. The flutter speed of the baseline design decreases for increasing root angle of attack, which eventually causes an increase in the mass of the optimized design. This behavior is caused by the change in the flutter mode between $\alpha = 0°$ and $\alpha = 3°$ and by the more pronounced instability of the new critical mode between $\alpha = 3°$ and $\alpha = 6°$ (Table 5).

6 Conclusions

This paper presented a framework for high-fidelity gradient-based wing structural optimization subject to a geometrically nonlinear flutter constraint. The framework evaluates the mass objective function and the linear stress and adjacency constraints on a built-up (detailed) FEM to capture realistic structural details. The built-up FEM at each optimization step is condensed to a low-order equivalent beam model to keep the geometrically nonlinear flutter constraint computationally tractable for optimization. The geometrically nonlinear flutter analysis considers the wing statically deformed shape at each flight condition, and KS-aggregates the damping values into a scalar constraint.

The methodology was implemented into a computational environment that couples the built-up FEM solver TACS with the nonlinear aeroelastic solver UM/NAST using UM/EF2S to reduce the built-up FEM to a beam model at each optimization step. The total derivatives of the geometrically

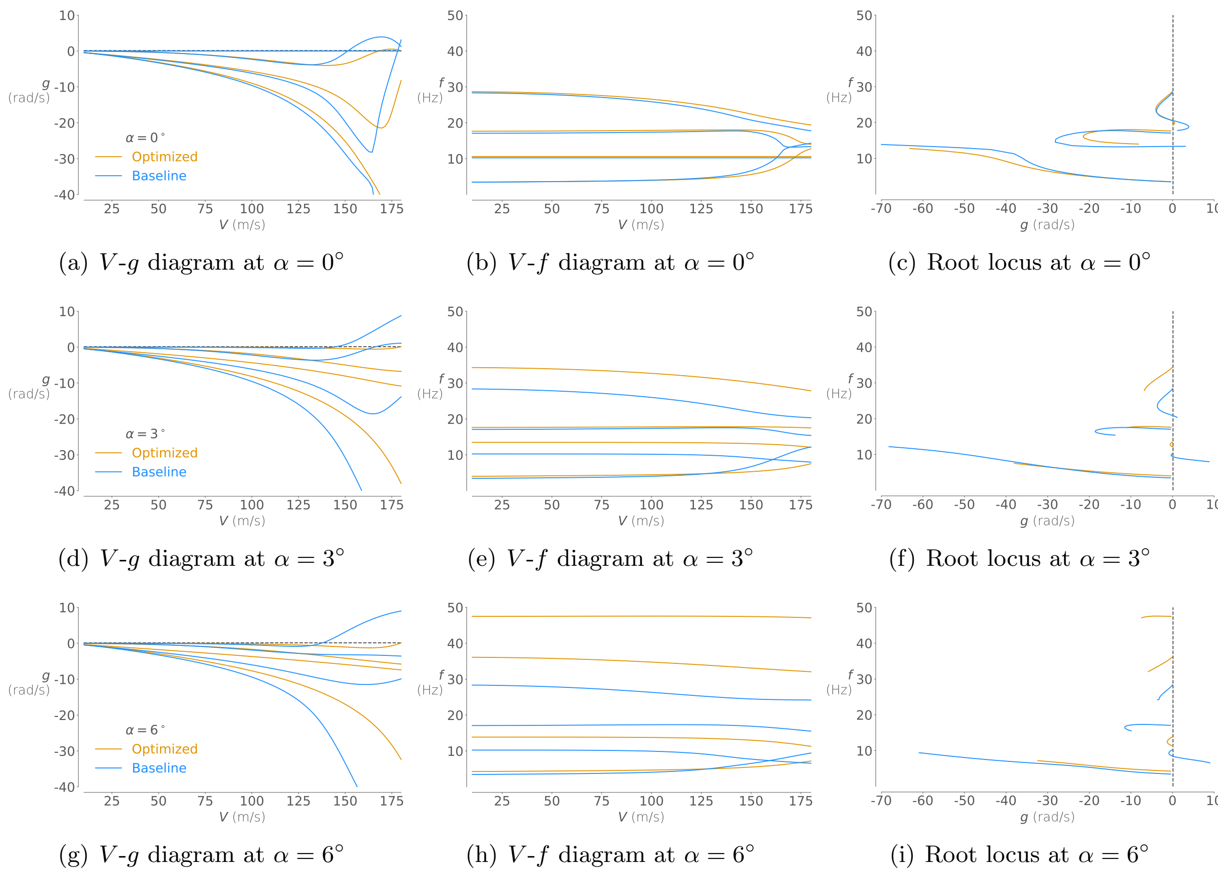

(a) V-g diagram at $\alpha = 0°$ (b) V-f diagram at $\alpha = 0°$ (c) Root locus at $\alpha = 0°$

(d) V-g diagram at $\alpha = 3°$ (e) V-f diagram at $\alpha = 3°$ (f) Root locus at $\alpha = 3°$

(g) V-g diagram at $\alpha = 6°$ (h) V-f diagram at $\alpha = 6°$ (i) Root locus at $\alpha = 6°$

Figure 9: Flutter analysis of baseline and optimized designs for each root angle of attack.

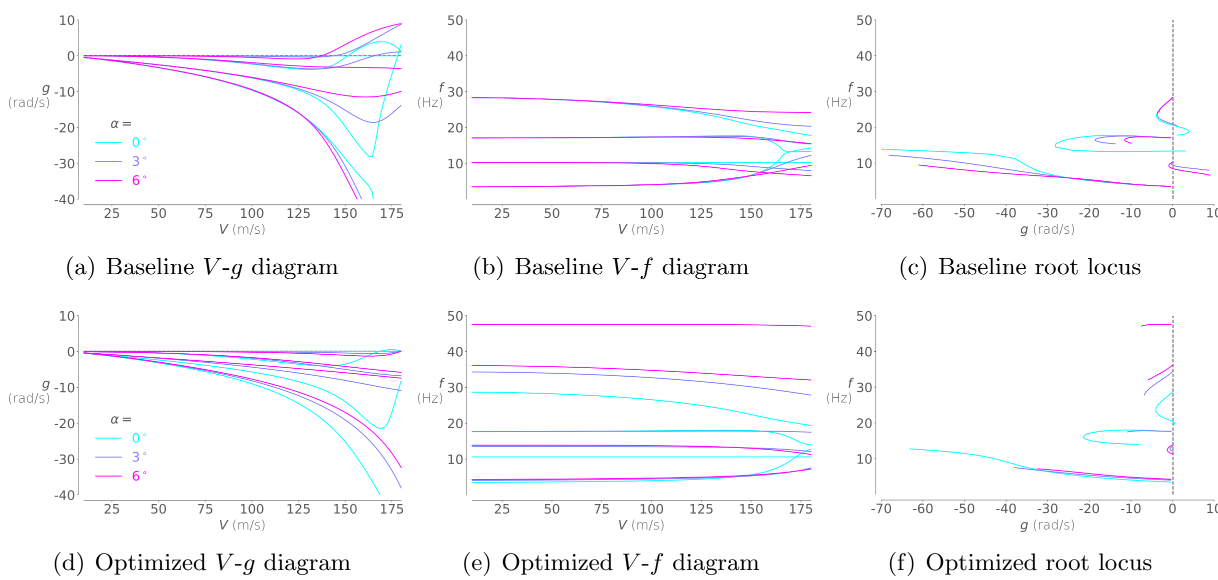

(a) Baseline V-g diagram (b) Baseline V-f diagram (c) Baseline root locus

(d) Optimized V-g diagram (e) Optimized V-f diagram (f) Optimized root locus

Figure 10: Flutter analysis of all baseline and optimized designs.

nonlinear flutter constraint evaluated on the beam model with respect to the detailed structural sizing variables were computed using the adjoint method.

The methodology was demonstrated by minimizing the mass of a high-aspect-ratio wingbox subject to the geometrically nonlinear flutter constraint along with stress and adjacency constraints. Multiple optimizations were performed with the flutter constraint computed at different root angles of attack to explore the impact of geometrically nonlinear effects. In all optimizations, the stress constraints were evaluated considering pre-computed loads representative of a 2.5-g maneuver to focus on the effect of the flutter constraint.

At nonzero root angle of attack, the flutter constraint added a mass penalty up to more than five times the one at zero root angle of attack, where the wing is undeformed in the flutter analysis. The mass increase with the root angle of attack is attributed to the impact of wing static aeroelastic deflections on the flutter speed and mechanism, which is associated with the geometrically nonlinear effect. The optimized designs showed significantly different thickness distributions as the optimizer sought to mitigate a 3-DOF flutter mechanism that only occurs when wing deflections are considered.

These results demonstrate the need for geometrically nonlinear flutter analyses when optimizing wings with high aspect ratios subject to a flutter constraint. This work fills a gap left by previous efforts, which either optimized a built-up FEM based on a linear flutter constraint or included geometrically nonlinear effects but only optimized a beam model. Furthermore, This work is a step toward considering geometrically nonlinear flutter analyses early in the aircraft design cycle.

Acknowledgments

The material of this paper is based upon work supported by Airbus in the frame of the Airbus-Michigan Center for Aero-Servo-Elasticity of Very Flexible Aircraft (CASE-VFA). The authors thank Patrick Teufel (Airbus Operations GmbH) for his review of the paper and for the technical discussions throughout this work.

References

[1] Afonso, F., Vale, J., Oliveira, É., Lau, F., and Suleman, A., "A Review on Non-Linear Aeroelasticity of High Aspect-Ratio Wings," *Progress in Aerospace Sciences*, Vol. 89, No. Supplement C, 2017, pp. 40–57. doi:10.1016/j.paerosci.2016.12.004.

[2] Cesnik, C. E. S., Palacios, R., and Reichenbach, E. Y., "Reexamined Structural Design Procedures for Very Flexible Aircraft," *Journal of Aircraft*, Vol. 51, No. 5, 2014, pp. 1580–1591. doi:10.2514/1.C032464.

[3] Patil, M. J., Hodges, D. H., and Cesnik, C. E. S., "Limit-Cycle Oscillations in High-Aspect-Ratio Wings," *Journal of Fluids and Structures*, Vol. 15, No. 1, 2001, pp. 107–132. doi:10.1006/jfls.2000.0329.

[4] Patil, M. J., Hodges, D. H., and Cesnik, C. E. S., "Nonlinear Aeroelasticity and Flight Dynamics of High-Altitude Long-Endurance Aircraft," *Journal of Aircraft*, Vol. 38, No. 1, 2001, pp. 88–94. doi:10.2514/2.2738.

[5] Patil, M. J., and Hodges, D. H., "Flight Dynamics of Highly Flexible Flying Wings," *Journal of Aircraft*, Vol. 43, No. 6, 2006, pp. 1790–1799. doi:10.2514/1.17640.

[6] Su, W., and Cesnik, C. E. S., "Nonlinear Aeroelasticity of a Very Flexible Blended-Wing-Body Aircraft," *Journal of Aircraft*, Vol. 47, No. 5, 2010, pp. 1539–1553. doi:10.2514/1.47317.

[7] Su, W., and Cesnik, C. E. S., "Dynamic Response of Highly Flexible Flying Wings," *AIAA Journal*, Vol. 49, No. 2, 2011, pp. 324–339. doi:10.2514/1.53412.

[8] Jonsson, E., Riso, C., Lupp, C. A., Cesnik, C. E. S., Martins, J. R. R. A., and Epureanu, B. I., "Flutter and Post-Flutter Constraints in Aircraft Design Optimization," *Progress in Aerospace Sciences*, Vol. 109, 2019, pp. 1–28. doi:10.1016/j.paerosci.2019.04.001.

[9] Bartels, R. E., and Stanford, B. K., "Aeroelastic Optimization with an Economical Transonic Flutter Constraint Using Navier–Stokes Aerodynamics," *Journal of Aircraft*, Vol. 55, No. 4, 2018, pp. 1522–1530. doi:10.2514/1.C034675.

[10] He, S., Jonsson, E., and Martins, J. R., "Wing Aerodynamic Shape Optimization with Time Spectral Limit-Cycle Oscillation Adjoint," *AIAA AVIATION 2022 Forum*, 2022. doi:10.2514/6.2022-3357, URL https://arc.aiaa.org/doi/abs/10.2514/6.2022-3357.

[11] Jacobson, K., and Stanford, B., "Flutter-Constrained Optimization with the Linearized Frequency-Domain Approach," *AIAA SCITECH 2022 Forum*, 2022. doi:10.2514/6.2022-2242, URL https://arc.aiaa.org/doi/abs/10.2514/6.2022-2242.

[12] Werter, N. P., and De Breuker, R., "A novel dynamic aeroelastic framework for aeroelastic tailoring and structural optimisation," *Composite Structures*, Vol. 158, 2016, pp. 369–386. doi:10.1016/j.compstruct.2016.09.044, URL http://dx.doi.org/10.1016/j.compstruct.2016.09.044.

[13] Rajpal, D., Gillebaart, E., and De Breuker, R., "Preliminary aeroelastic design of composite wings subjected to critical gust loads," *Aerospace Science and Technology*, Vol. 85, 2019, pp. 96–112. doi:10.1016/j.ast.2018.11.051, URL https://doi.org/10.1016/j.ast.2018.11.051.

[14] Krüger, W. R., Dillinger, J., De Breuker, R., and Haydn, K., "Investigations of passive wing technologies for load reduction," *CEAS Aeronautical Journal*, Vol. 10, No. 4, 2019, pp. 977–993. doi:10.1007/s13272-019-00393-2, URL https://doi.org/10.1007/s13272-019-00393-2.

[15] Variyar, A., Economon, T. D., and Alonso, J. J., "Design and Optimization of Unconventional Aircraft Configurations with Aeroelastic Constraints," *2017 AIAA SciTech Forum*, Grapevine, TX, 2017, pp. 1–13. doi:10.2514/6.2017-0463, aIAA-2017-0463.

[16] Xie, C., Meng, Y., Wang, F., and Wan, Z., "Aeroelastic Optimization Design for High-Aspect-Ratio Wings with Large Deformation," *Shock and Vibration*, 2017, pp. 1–16. doi:10.1155/2017/2564314.

[17] Lupp, C. A., and Cesnik, C. E. S., "A Gradient-Based Flutter Constraint Including Geometrically Nonlinear Deformations," *2019 AIAA SciTech Forum*, San Diego, CA, 2019, pp. 1–22. doi:10.2514/6.2019-1212.

[18] Goizueta, N., Wynn, A., Palacios, R., Drachinsky, A., and Daniella, R., "Flutter Predictions for Very Flexible Wing Wind Tunnel Test," *Journal of Aircraft*, 2022, pp. 1–16. doi:10.2514/1.C036710, article in advance.

[19] Riso, C., and Cesnik, C. E. S., "Impact of Low-Order Modeling on Aeroelastic Predictions for Very Flexible Wings," *Journal of Aircraft*, 2022. doi:10.2514/1.C036869, to appear.

[20] Jonsson, E., Mader, C. A., Kennedy, G. J., and Martins, J. R. R. A., "Computational Modeling of Flutter Constraint for High-Fidelity Aerostructural Optimization," *2019 AIAA SciTech Forum*, San Diego, CA, 2019, pp. 1–27. doi:10.2514/6.2019-2354, aIAA-2019-2354.

[21] Martins, J. R. R. A., and Ning, A., *Engineering Design Optimization*, Cambridge University Press, 2021. doi:10.1017/9781108980647, URL https://mdobook.github.io.

[22] Su, W., and Cesnik, C. E. S., "Strain-Based Geometrically Nonlinear Beam Formulation for Modeling Very Flexible Aircraft," *International Journal of Solids and Structures*, Vol. 48, No. 16–17, 2011, pp. 2349–2360. doi:10.1016/j.ijsolstr.2011.04.012.

[23] Hinton, E., Rock, T., and Zienkiewicz, O. C., "A note on mass lumping and related processes in the finite element method," *Earthquake Engineering & Structural Dynamics*, Vol. 4, No. 3, 1976, pp. 245–249. doi:https://doi.org/10.1002/eqe.4290040305.

[24] Cesnik, C. E. S., and Hodges, D. H., "VABS: A New Concept for Composite Rotor Blade Cross-Sectional Modeling," *Journal of the American Helicopter Society*, Vol. 42, No. 1, 1997, pp. 27–38. doi:10.4050/jahs.42.27.

[25] Riso, C., Sanghi, D., Cesnik, C. E. S., Vetrano, F., and Teufel, P., "Parametric Nonlinear Aeroelastic Analysis of a High-Aspect-Ratio-Wing Civil Transport Aircraft," *2020 AIAA SciTech Forum*, Orlando, FL, 2020, pp. 1–23. doi:10.2514/6.2020-1191, AIAA-2020-1191.

[26] Riso, C., and Cesnik, C. E. S., "Correlations between UM/NAST Nonlinear Aeroelastic Simulations and the Pre-Pazy Wing Experiment," *2021 AIAA SciTech Forum*, Virtual Event, 2021, pp. 1–24. doi:10.2514/6.2021-1712, AIAA-2021-1712.

[27] Peters, D. A., Hsieh, M. C. A., and Torrero, A., "A State-Space Airloads Theory for Flexible Airfoils," *Journal of the American Helicopter Society*, Vol. 52, No. 4, 2007, pp. 329–342. doi:10.4050/JAHS.52.329.

[28] Riso, C., and Cesnik, C. E. S., "Low-Order Geometrically Nonlinear Aeroelastic Modeling and Analysis of the Pazy Wing Experiment," *2022 AIAA SciTech Forum*, San Diego, CA & Online, 2022, pp. 1–30. doi:10.2514/6.2022-2313, AIAA-2022-2313.

[29] Kreisselmeier, G., and Steinhauser, R., "Systematic Control Design by Optimizing a Vector Performance Index," *Computer Aided Design of Control Systems*, Pergamon, 1980, pp. 113–117. doi:10.1016/B978-0-08-024488-4.50022-X.

[30] Wrenn, G. A., "An Indirect Method for Numerical Optimization Using the Kreisselmeier–Steinhauser Function," Tech. rep. cr-4220, NASA Langley Research Center, Hampton, VA, 1989.

[31] Poon, N. M. K., and Martins, J. R. R. A., "An Adaptive Approach to Constraint Aggregation using Adjoint Sensitivity Analysis," *Structural and Multidisciplinary Optimization*, Vol. 34, 2007, pp. 61–73. doi:10.1007/s00158-006-0061-7.

[32] Kennedy, G. J., and Martins, J. R. R. A., "A Parallel Finite-Element Framework for Large-Scale Gradient-Based Design Optimization of High-Performance Structures," *Finite Elements in Analysis and Design*, Vol. 87, 2014, pp. 56–73. doi:10.1016/j.finel.2014.04.011.

[33] Gill, P. E., Murray, W., and Saunders, M. A., "SNOPT: An SQP Algorithm for Large-Scale Constrained Optimization," *SIAM Journal of Optimization*, Vol. 12, No. 4, 2002, pp. 979–1006. doi:10.1137/S1052623499350013.

[34] Wu, N., Kenway, G., Mader, C. A., Jasa, J., and Martins, J. R. R. A., "pyOptSparse: A Python framework for Large-Scale Constrained Nonlinear Optimization of Sparse Systems," *Journal of Open Source Software*, Vol. 5, No. 54, 2020, p. 2564. doi:10.21105/joss.02564.

[35] Perez, R. E., Jansen, P. W., and Martins, J. R. R. A., "pyOpt: A Python-Based Object-Oriented Framework for Nonlinear Constrained Optimization," *Structural and Multidisciplinary Optimization*, Vol. 45, No. 1, 2012, pp. 101–118. doi:10.1007/s00158-011-0666-3.

[36] Kennedy, G. J., and Martins, J. R. R. A., "A Parallel Aerostructural Optimization Framework for Aircraft Design Studies," *Structural and Multidisciplinary Optimization*, Vol. 50, No. 6, 2014, pp. 1079–1101. doi:10.1007/s00158-014-1108-9.

[37] Gray, J. S., Hwang, J. T., Martins, J. R. R. A., Moore, K. T., and Naylor, B. A., "OpenMDAO: An Open-Source Framework for Multidisciplinary Design, Analysis, and Optimization," *Structural and Multidisciplinary Optimization*, Vol. 59, No. 4, 2019, pp. 1075–1104. doi:10.1007/s00158-019-02211-z.

[38] Skujins, T., and Cesnik, C. E. S., "Reduced-order Modeling of Unsteady Aerodynamics Across Multiple Mach Regimes," *Journal of Aircraft*, Vol. 51, No. 6, 2014. doi:10.2514/1.C032222.

[39] Mader, C. A., Kenway, G. K. W., Yildirim, A., and Martins, J. R. R. A., "ADflow: An Open-Source Computational Fluid Dynamics Solver for Aerodynamic and Multidisciplinary Optimization," *Journal of Aerospace Information Systems*, Vol. 17, No. 9, 2020, pp. 508–527. doi:10.2514/1.I010796.

[40] Stroud, W. J., and Agranoff, N., "Minimum-Mass Design of Filamentary Composite Panels Under Combined Loads: Design Procedure Based on Simplified Buckling Equations," Tech. Rep. TN-D-8257, NASA Langley Research Center, Hampton, VA, 1976.

[41] Kennedy, G. J., Kenway, G. K. W., and Martins, J. R. R. A., “High Aspect Ratio Wing Design: Optimal Aerostructural Tradeoffs for the Next Generation of Materials,” *Proceedings of the AIAA Science and Technology Forum and Exposition (SciTech)*, National Harbor, MD, 2014. doi:10.2514/6.2014-0596.